



Cite as
Nano-Micro Lett.
(2023) 15:82

Received: 25 December 2022
Accepted: 28 February 2023
Published online: 31 March 2023
© The Author(s) 2023

Rational Design of High-Performance PEO/Ceramic Composite Solid Electrolytes for Lithium Metal Batteries

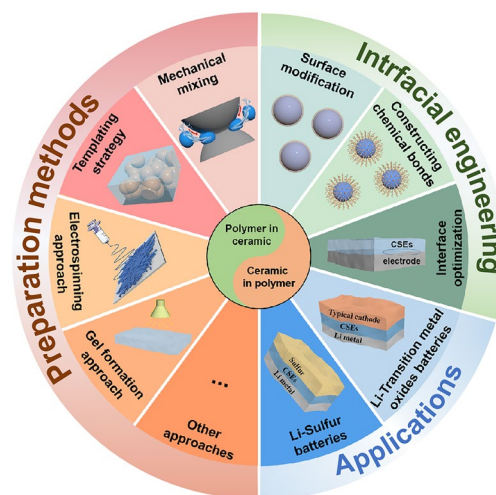
Yanxia Su¹, Fei Xu¹ ✉, Xinren Zhang¹, Yuqian Qiu¹, Hongqiang Wang¹ ✉

HIGHLIGHTS

- The design, preparation and application of poly(ethylene oxide) (PEO)/ceramic composite solid electrolytes (CSEs) are summarized from “ceramic in polymer” and “polymer in ceramic”.
- The summary and outlook on existing challenges and future research directions of PEO/ceramic CSEs for lithium metal batteries are proposed.

ABSTRACT Composite solid electrolytes (CSEs) with poly(ethylene oxide) (PEO) have become fairly prevalent for fabricating high-performance solid-state lithium metal batteries due to their high Li⁺ solvating capability, flexible processability and low cost. However, unsatisfactory room-temperature ionic conductivity, weak interfacial compatibility and uncontrollable Li dendrite growth seriously hinder their progress. Enormous efforts have been devoted to combining PEO with ceramics either as fillers or major matrix with the rational design of two-phase architecture, spatial distribution and content, which is anticipated to hold the key to increasing ionic conductivity and resolving interfacial compatibility within CSEs and between CSEs/electrodes. Unfortunately, a comprehensive review exclusively discussing the design, preparation and application of PEO/ceramic-based CSEs is largely lacking, in spite of tremendous reviews dealing with a broad spectrum of polymers and ceramics. Consequently, this review targets recent advances in PEO/ceramic-based CSEs, starting with a brief introduction, followed by their ionic conduction mechanism, preparation methods, and then an emphasis on resolving ionic conductivity and interfacial compatibility. Afterward, their applications in solid-state lithium metal batteries with transition metal oxides and sulfur cathodes are summarized. Finally, a summary and outlook on existing challenges and future research directions are proposed.

KEYWORDS Composite solid electrolytes; Ionic conductivity; Interfacial compatibility; Ion conduction pathways; Li metal batteries



✉ Fei Xu, feixu@nwpu.edu.cn; Hongqiang Wang, hongqiang.wang@nwpu.edu.cn

¹ State Key Laboratory of Solidification Processing, Centre for Nano Energy Materials, School of Materials Science and Engineering, Northwestern Polytechnical University, Shaanxi Joint Laboratory of Graphene (NPU), Xi'an 710072, People's Republic of China



1 Introduction

Currently, clean and sustainable energy is one of the most important issues for economic development worldwide [1]. Thus, energy storage and conversion are becoming more indispensable than ever before, especially with the fast increase in global population and worldwide development [2–5]. Rechargeable lithium-ion batteries (LIBs) have a high gravimetric and volumetric energy density compared with the other types of commercially available rechargeable battery technologies for electrochemical energy storage, and thus they have been extensively used in portable devices, electric vehicles, and grid energy storage since their first commercialization by Sony in 1991 [6–8]. However, state-of-the-art commercial LIB devices gradually cannot meet the increasing demand for powering a range of electric vehicles and large-scale grid energy storage [9, 10], due to the limited energy density ($< 200 \text{ Wh kg}^{-1}$) with current electrode materials like LiFePO_4 cathode and graphite anode. Compared to the theoretical capacity of 372 mAh g^{-1} for the graphite anode in commercial LIBs, the lithium metal anode shows a much higher theoretical capacity (3860 mAh g^{-1}). Meanwhile, it shows the lowest reduction potential (-3.04 V vs. standard hydrogen electrode), thus allowing a high voltage in full battery devices [11, 12]. Consequently, lithium metal batteries (LMBs) with Li metal anodes could achieve a much higher energy density originating from both large capacity and high full cell voltage windows. However, the practical use of LMBs is seriously hindered by uncontrollable dendrite growth, unstable electrolyte/Li interface and thus poor cycle stability [10, 13]. Meanwhile, the flammable and volatile organic liquid electrolytes used in conventional LMBs give rise to safety concerns (e.g., fire or explosion), especially with the occurrence of short circuits induced by Li dendrite formation [14–16]. Furthermore, they also show unsatisfactory stability against high voltage cathodes ($> 4.5 \text{ V}$) and suffer from side reactions, aggravating the capacity and lifespan degradation [17, 18]. Therefore, it is necessary to develop efficient electrolyte systems beyond the liquid ones, which could allow dendrite-free Li anodes and safe operation while delivering long-cycle stability and tolerance to high voltage cathodes.

In this context, solid-state electrolytes and gel electrolytes have recently drawn sufficient attention as a potential substitute for organic liquid electrolytes in terms of safety and Li

dendrite suppression [19–21]. Gel electrolytes have higher ionic conductivity due to the presence of liquid component, but poor mechanical strength and the possibility of uncontrolled thermal runaway. However, solid-state electrolytes have sufficient mechanical strength and higher security [22, 23]. Therefore, solid-state electrolytes could revive the possibility of using a high-energy-density Li metal anode, which is mainly divided into three categories according to their composition: solid ceramic electrolytes [24, 25], solid polymer electrolytes [26, 27] and composite solid electrolytes (CSEs) [28–30]. CSEs are unique in that they can merge the advantages of both solid ceramic electrolytes and solid polymer electrolytes, thus exhibiting better ionic conductivity, higher compatibility with electrodes and enhanced mechanical tolerance [31, 32]. A typical CSE is composed of polymers solvating lithium salts and inorganic ceramics in various architectures [33]. Inorganic ceramics can be either Li^+ insulative, such as TiO_2 [34, 35], Al_2O_3 [36], SiO_2 [37] or Li^+ conductive, including $\text{Li}_{1.3}\text{Al}_{0.3}\text{Ti}_{1.7}(\text{PO}_4)_3$ (LATP) [38, 39], $\text{Li}_{10}\text{GeP}_2\text{S}_{12}$ (LGPS) [40], $\text{Li}_7\text{La}_3\text{Zr}_2\text{O}_{12}$ (LLZO) [41, 42], LiTa_2PO_8 (LTPO) [43], etc. Various ceramic matrix/fillers exhibit different effects on CSEs due to the nature of ceramics. From the viewpoint of ionic conductivity, conductive ceramics work better than insulative ones. However, Li^+ insulative ceramic fillers generally show the advantages of low cost and adaptable processability. For those conductive ceramics sulfides exhibit ionic conductivity up to $10^{-3} \text{ S cm}^{-1}$ and low grain boundary resistance at room temperature due to the large size and polarization of sulfide ions. In contrast, oxides (LLZO, LIPON) have better oxidation resistance than sulfides due to kinetic stability, and garnet LLZO (cubic phase) shows the highest resistance to being reduced by lithium. The polymers used generally include poly(vinylidene fluoride) (PVDF) [44, 45], poly(ethylene oxide) (PEO) [46, 47], polyacrylonitrile (PAN) [37], poly(vinylidene fluoride-hexafluoropropylene) (PVDF-HFP), etc. [48], and Li salts include LiClO_4 [49], LiTFSI [50], LiFSI [51], etc. PVDF has good dielectric constant and high interfacial stability with lithium metal, while possess lower ionic conductivity at room temperature [52]. PAN has good stability with high-voltage cathode, but poor stability with lithium metal [53]. Among various CSEs, polymers using PEO are unique in that they possess higher Li^+ solvating capability, flexibility, processability and low cost [27].

Since the first discovery of the ionic conductivity of PEO by Wright et al. [54] in 1973, PEO-based solid-state electrolytes have been extensively studied [55, 56]. The transportation of Li^+ is mainly dominated by the segmental relaxation of PEO chains, and thus, the high crystallinity of PEO gives rise to the limited ionic conductivities ($< 10^{-5} \text{ S cm}^{-1}$) and low Li^+ transference numbers (0.2–0.4) at room temperature [57]. Meanwhile, the poor mechanical strength and the vulnerability against oxidation of PEO (no more than 4.0 V) further impede their practical applications, especially for high-voltage solid-state LMBs [58, 59]. To overcome these shortcomings, the combination of ceramics and PEO is anticipated to achieve better electrolytes delivering simultaneously attractive ionic conductivity, high voltage tolerance and good mechanical strength. As early as 1998, Croce et al. [60] firstly demonstrated that the Li^+ conductivity can be improved to $10^{-4} \text{ S cm}^{-1}$ at 50°C and $10^{-5} \text{ S cm}^{-1}$ at 30°C by incorporating TiO_2 and Al_2O_3 as filler into PEO with LiClO_4 salt, respectively. Encouraged by this pioneering work, much effort has been devoted to optimizing the ionic conductivity as well as the compatibility for practical CSEs in LMBs [61, 62].

Benefitting from these advantages of PEO, such as, low density and interface impedance, easy to thin layer and machining, PEO and its derived CSEs become one of the most commercial prospect electrolyte materials. The PEO electrolyte was the first to promote commercialization by Bollore [63] Company in 2011, achieving the electric vehicle with solid-state battery as the power system (110 Wh kg^{-1} at $70\text{--}80^\circ\text{C}$). Unfortunately, low ionic conductivity at room temperature limits energy density and enables energy consumption and cost after heating up. Therefore, a review focused on discussing the design, preparation and application of PEO/ceramic CSEs is required, especially for identifying conduction mechanisms and realizing performance optimization, furtherly promoting cost-efficient production. Thus, we specifically reviewed PEO/ceramic CSEs, which is different from the recent large number of reviews focusing on various polymer/ceramic CSEs [29, 57, 62, 64–70]. In this review, beginning with a brief introduction to solid-state electrolytes and especially for PEO/ceramic CSEs, the Li^+ conduction mechanism is analyzed with architectures from “ceramic in polymer” to “polymer in ceramic”. Then, preparation methods are summarized, including mechanical mixing, templating strategies, electrospinning and gel formation approaches, along with discussions of their respective

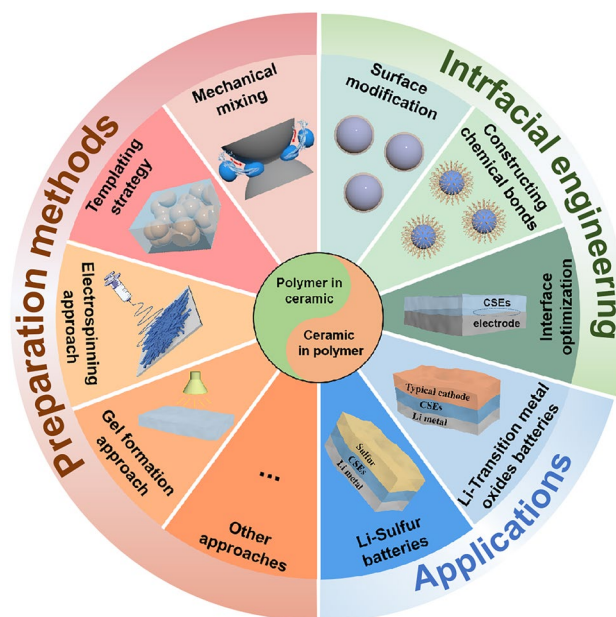


Fig. 1 The organization of this review scheme

cons and pros for developing high-quality PEO/ceramic CSEs. Subsequently, interface regulation and architecture design within PEO/ceramic CSEs and between CSEs/electrodes are emphasized to optimize interfacial compatibility (Fig. 1). After that, the applications of PEO/ceramic CSEs paired with transition metal oxides and sulfur cathodes in solid-state lithium metal batteries are provided. Finally, a summary and outlook of PEO/ceramic CSEs are proposed. Hopefully, this review will engender interest in acquiring a basic understanding of PEO-based CSEs and stimulate further explorations even for beginners in the ion conduction mechanism, design strategies and Li metal full cells with high ion conductivity, superior compatible with cathode and anode, and ultrathin thickness yet mechanical stability.

2 Li^+ Conduction Mechanism

The Li^+ conductivity is one of the most important parameters in CSEs. An insightful understanding of the Li^+ conduction mechanism or behavior is critical to realizing high ionic conductivity, which is closely associated with the relative ratio and architecture of PEO and ceramic [71–73]. Moreover, advanced characterization techniques are key to studying the local structural environments and dynamics of lithium ions.

2.1 Effects of Architecture on Li⁺-Conducting Pathways

The conduction mechanism of PEO–Li can be generalized by the combination and dissociation of EO–Li bonds, together with the main chain movement of PEO. Li⁺ can be transported on a single chain or between different chains. The Li⁺ migration depends on the movement of polymer chains and mainly occurs in the amorphous region. However, PEO is easy to form crystalline phase at room temperature, which hinders chain movement and thus Li⁺ migration. Therefore, the operating temperature of solid-state batteries is usually higher than the melting temperature of PEO (>65 °C) [66]. However, PEO homopolymer is a viscous liquid, and its mechanical properties are too weak to slow down the growth of lithium dendrites during cycling. Many methods have been explored to improve ionic conductivity and mechanical properties of PEO-based solid polymer electrolytes. It is found that the adding of inorganic fillers can promote the formation of local amorphous regions, thus promoting Li⁺ transfer [74].

According to the report of Goodenough, CSEs can be divided into two categories, “ceramic in polymer” and “polymer in ceramic” [75]. In the former system, ceramic serves as a filler (minor phase) in the PEO–Li salt complex matrix to increase the Li⁺ conductivity, whereas in the latter system, the addition of PEO–Li salt in the ceramic matrix can improve interface compatibility [38, 76]. The possible Li⁺ conduction pathways and conduction properties are summarized in Fig. 2, as discussed below [77, 78]. Generally, there are three possible Li⁺ conduction pathways, including in the PEO phase, at PEO/ceramic interface and in the ceramic phase [79].

In the “ceramic in polymer” system, ceramic fillers help to suppress the crystallization of PEO chains [77, 80]. The lower the crystallinity is, the higher the Li⁺ transportation ability because better crystallinity could decrease the free volume with more compact packing of parallel polymer chains against Li⁺ transportation [33, 61]. Therefore, the incorporation of fillers in PEO could enhance the ionic conductivity by the generation of more amorphous regions for facile segment movement. Fillers such as nanoparticles

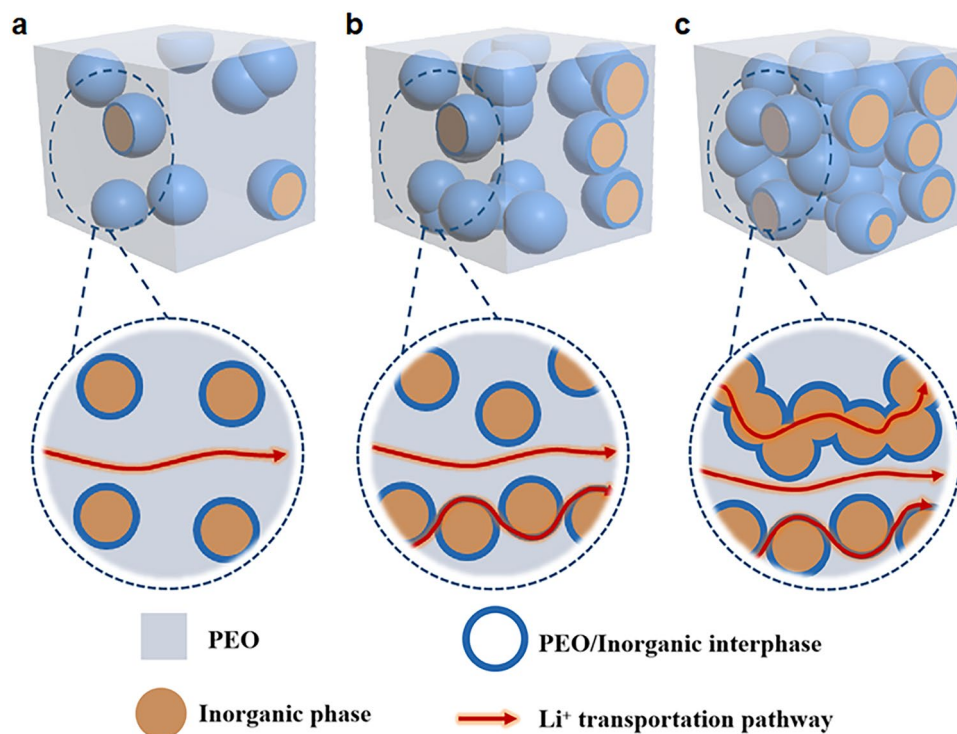


Fig. 2 Schematic illustration of the Li⁺ conduction pathways **a** in the PEO phase, **b** in the PEO phase and at PEO/ceramic interface, and **c** in the PEO phase and ceramic phase and at PEO/ceramic interface

are generally discontinuously dispersed in the PEO matrix (Fig. 2a). In this context, Li^+ conduction pathways are mainly governed by the motion within the PEO phase, no matter whether the fillers are inert or conductive for lithium ions [28, 57]. This was confirmed experimentally by increasing the fraction of ceramics in CSEs, in which Li^+ conduction pathways transfer from PEO to the PEO/ceramic interface, which plays a vital role in regulating Li^+ conduction in PEO-based CSEs (Fig. 2b) [77]. In addition to the typical nanoparticle fillers, different morphologies, such as nanowire and nanosheet fillers, have also been used [81]. It was reported that nanowire fillers not only favor the generation of amorphous regions but also offer continuous active pathways along the interfaces for fast Li^+ transportation and superior ionic conductivity compared to nanoparticles [82, 83]. Moreover, well-aligned inorganic Li^+ conductive nanowires were reported to show favorable for Li^+ conduction than randomly aligned nanowires [84]. Nanosheet fillers such as C_3N_4 [85], BN [86], MXene [81, 87] or vermiculite [88] have been used, which are expected to offer a higher surface area and provide continuous 2D interfaces between the fillers and the polymer matrix, thus ensuring rapid diffusion of lithium ions [89–91]. Exploration of a broader range of nanosheet fillers is still needed with both electron insulation and chemical and thermal stability. The Li^+ conduction pathways in the “ceramic in polymer” configuration will influence the Li^+ conductivity. Generally, with increasing ceramic content, the ionic conductivity increases. The ionic conductivity reaches the maximum at the percolation threshold, such as 10 wt% LLZTO [75], 25 wt% LATP [92], 20 wt% LAGP [93], 5 wt% MnO_2 [90] and 7.5 wt% TiO_2 [94]. However, further increasing the ceramic content will block ion transmission and cause a decrease in ionic conductivity. Bouchet et al. [95] also verified the conclusion via using CSEs model system. The size of ceramic fillers also influences the percolation threshold [96]. Compared with corresponding bulk fillers, nanofillers could provide a higher surface area, sufficient interfacial contact sites with PEO, and thus a low percolation effect and smooth ion conduction pathways. For example, Liu et al. [97] developed 200 nm LLZTO and found that the percolation threshold is 20 wt% showing the best ionic conductivity. Likewise, a 100 nm LLZTO nanoparticle as filler shows a value of 11.53 wt% [98]. Recently, we prepared 8.3 nm LLZTO nanoparticles by laser manufacturing in liquid, and the percolation threshold is down to 2 wt%, which is one of the

record values among PEO-based electrolytes, to the best of our knowledge [80]. Apart from the above ceramic content and size, Li-salt content and ceramic species also impact the Li^+ conduction mechanisms. For example, the impact of LiTFSI content (EO/Li = 18:1, 9:1 and 6:1) on LGPS/PEO interface formation showed that low LiTFSI content has little effect on interface formation. The high LiTFSI content also has limited LGPS/PEO interface formation. This is because excess LiTFSI partially aggregates and the interaction between PEO and LiTFSI alters mechanical properties of PEO, showing poor interface compatibility with LGPS [72]. As compared with the Li^+ insulating ceramics, Li^+ -conducting ones improve Li^+ conductivity due to their ability to conduct Li^+ through the ceramic as well as across the interface [99]. Meanwhile, the Li^+ conductive filler $\text{LiZr}_2(\text{PO}_4)_3$ (LZP) allows more Li^+ reallocation in the disordered local environment of PEO, facilitating better Li^+ mobility and enhancing the ionic conductivity, superior to Li^+ insulative Al_2O_3 filler CSEs [78].

In contrast, in the “polymer in ceramic” system, PEO–Li salt complexes are embedded or confined into the continuous, tightly packed ceramic matrix (Fig. 2c). In most cases, ceramic matrix is Li^+ conductive, which not only helps suppress the crystallization of the PEO phase but also affords continuous Li^+ conduction pathways within the ceramic matrix and along the interfaces [43, 80]. Only in some few cases, the ceramics (e.g., SiO_2) is Li^+ -insulative, and thus the Li^+ is mainly transported along the continuous interface [100]. In these “polymer in ceramic” architectures, the continuous 3D garnet skeleton avoids agglomeration of ceramic particles and provides continuous conductive interfaces, thus improving the conductivity as compared with the isolated particles in polymer matrix, at their respective percolation threshold. For example, Guo et al. [101] reported that CSEs with 3D garnet skeleton showed an ionic conductivity of $1.2 \times 10^{-4} \text{ S cm}^{-1}$ at 30 °C, which was about two times that of garnet particle-reinforced polymer-based CSEs ($6.4 \times 10^{-5} \text{ S cm}^{-1}$).

2.2 Characterization Techniques

Various characterization tools are used to clarify Li^+ conduction pathways. Solid-state Li nuclear magnetic resonance (NMR) is one of the most powerful tools for studying local structural environments and the dynamic process of

Li^+ within CSEs using isotope exchange [102, 103]. This is realized by using a ^6Li labeled foil electrode to trace the ^6Li distribution in the original ^7Li -based CSEs via Li NMR due to the partial replacement of ^7Li with ^6Li during each cycle, thus enabling the clarification of Li^+ conduction pathways. As early as 2016, Hu et al. [104] reported the first experimental evidence of Li^+ conduction pathways using selective isotope labeling of solid-state Li NMR, and the result shows that Li^+ transportation prefers to go through the LLZO ceramic phase rather than the PEO/LLZO interface or PEO phase with 50 wt% LLZO (Fig. 3a–c). The LLZO content is critical to determine the Li^+ conduction pathways. As shown in Fig. 3d, Li^+ conduction pathways gradually transfer from the PEO phase to the percolated network made of loosely connected LLZO particles, by increasing the LLZO content (from 5 to 50 wt%) in CSEs [77]. Intriguingly, under 50 wt% LLZO in CSEs, the Li^+ conduction pathways can switch from the LLZO to the PEO phase by adding tetraethylene glycol dimethyl ether as a liquid plasticizer, which helps to increase the ion mobility in the PEO phase (Fig. 3d). When

the amount of the ceramic LGPS further increases to 70 wt% reaching the percolated network value, the Li^+ conduction pathways are in both LGPS and interfaces, different from 50% of LGPS with Li-ion transport mainly in LGPS. However, further increasing the LGPS content to 90%, the Li^+ transport mainly switches back to LGPS [105].

Furthermore, some in situ and ex situ characterization methods have been engaged to assist in the research of solid-state batteries, mainly including energy dispersive X-ray [106], scanning electron microscopy (SEM) [107], transmission electron microscopy (TEM) [108], Raman spectroscopy [109] and neutron depth profiling [103, 110]. Among those, in situ TEM is frequently employed with a high spatial resolution for studying the characteristics of the morphological evolution, phase transformations, chemical composite changes, interfacial behavior and solid electrolyte interphase and cathode electrolyte interphase formation in solid-state batteries, which has been documented in previous reviews for reference [111, 112].

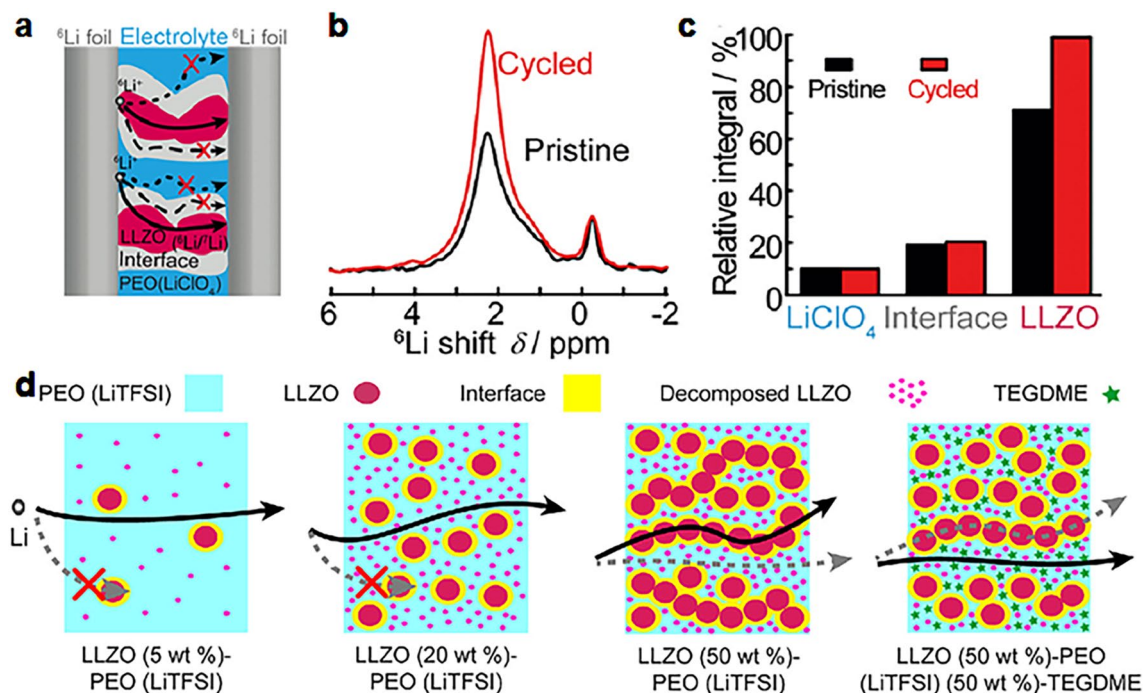


Fig. 3 **a** Illustration of the symmetric ^6Li battery and possible Li^+ conduction pathways. **b** Comparison of the ^6Li spectra of the LLZO/PEO(LiClO₄) electrolytes before and after cycling. **c** Quantitative analysis of the ^6Li amount in LiClO₄, the interface, and LLZO of LLZO/PEO(LiClO₄) before and after cycling. **a–c** Reproduced with permission [104]. Copyright 2016, Wiley–VCH. **d** Schematic of Li^+ pathways within CSEs. Reproduced with permission [77]. Copyright 2018, American Chemical Society

3 Preparation Methods of CSEs

The preparation methods are important to determine the architecture of CSEs and impact the ionic conductivity and electrochemical stability, which generally include mechanical mixing, templating strategies, electrospinning and gel formation approaches. Mechanical mixing is mainly applied for designing “ceramic in polymer” architectures, and composite films with thicknesses down to 30 μm can be obtained coupled with solution casting and hot pressing [113]. The templating strategy is propitious to the “polymers in ceramic” system, and the electrospinning approach is capable of fabricating nanowire membranes for both “ceramic in polymers” and “polymers in ceramic” systems. The gel formation approach can be used to design polymer-based gels for “ceramic in polymer” or ceramic-based gels for “polymer in ceramic” CSEs, which generally exhibit higher thickness (> 120 μm).

3.1 Mechanical Mixing

Mechanical mixing is one of the most prevalent methods to prepare CSEs, owing to its convenience and low cost. In this strategy, the PEO, Li salt or their predissolved solution was mixed with ceramic fillers via ball milling, sonification or stirring to make a well-dispersed suspension, followed by slurry casting and drying [92, 114–118]. Control over the PEO concentration is very important. The lower concentration will lead to difficulty in forming a film during casting, while the higher concentration will result in enhanced viscosity, thus impeding the uniform dispersion of ceramic fillers in the resulting composite electrolyte film. Compared with stirring and ultrasonic mixing, ball milling is advantageous for preparing a high-concentration mixture due to its high ball milling energy. For those solid ones without any organic solvent, hot pressing of the premixed mixture is adaptable [52, 119–122]. Nevertheless, the process of solid–solid mixing makes it difficult to mix inorganic ceramics and polymers well for forming a uniform CSE film [75]. The thickness of composite films can be regulated by the viscosity of the slurry or the pressure and temperature during hot pressing, which is currently as low as 30 μm [113].

Despite the convenience and low cost, mechanical mixing suffers from the aggregation of ceramic fillers, especially for those with nanosized and high concentrations. In

this regard, the ionic conductivity of CSEs cannot be efficiently enhanced due to the lack of sufficient interfaces for decreasing the PEO crystallinity. Meanwhile, filler aggregation also causes local differences in conductivity, leading to inhomogeneous Li-ion reflux in the bulk PEO substrate and thus the generation of Li dendrites [35, 123]. With the further increase in ceramic filler content (e.g., > 30 wt%), no continuous ceramic phase is generated, in contrast to the polymer in the ceramic architecture showing continuous Li⁺ conduction channels. Consequently, Li⁺ transport is blocked, causing a decrease in Li⁺ conductivity in this case [120, 124]. Therefore, there exists a percolation threshold for the ceramic filler content to realize a maximum Li⁺ conductivity, such as 2 wt% for Nano-LLZTO [80], 20 wt% for sheet-like Li_{6.25}La₃Zr₂Al_{0.25}O₁₂ (LLZAO) [89], 5 wt% for SiO₂ [125] and 25 wt% for LATP [92] and LiZr₂(PO₄)₃ [78]. To pursue facilitated conductivity under heavy ceramic content, the design of polymer in ceramic architecture is necessary, as discussed below by templating strategy and others.

3.2 Templating Strategy

As mentioned above, constructing polymer in ceramic architectures is promising to solve the issue of ceramic particle agglomeration but in isolated forms in PEO, especially at high concentrations [101]. The templating strategy is an effective way to fabricate CSEs with continuous ceramic skeleton, which involves two major steps: (1) the formation of a porous ceramic framework assisted with a template and (2) infiltration of PEO–Li salt solution, as shown in Fig. 4a with silk fabrics as templates [126]. The frequently used templates include silk [127], cotton [128], wood [129], textile cellulose [130], polystyrene microspheres [131], clean-room wiper [132], etc., which were infiltrated with ceramic precursors, followed by high-temperature calcination for template removal and final the formation of the ceramic framework. Subsequently, the preprepared PEO–Li salt solution is impregnated into the porous ceramic framework to obtain the CSEs by drying in a vacuum to remove the solvent.

There are several characteristics of the successful preparation of polymer in ceramic architecture CSEs via a templating strategy. First, the continuous porous structure of the template is required for forming a 3D consecutive inorganic ceramic skeleton, which is anticipated to provide better ion

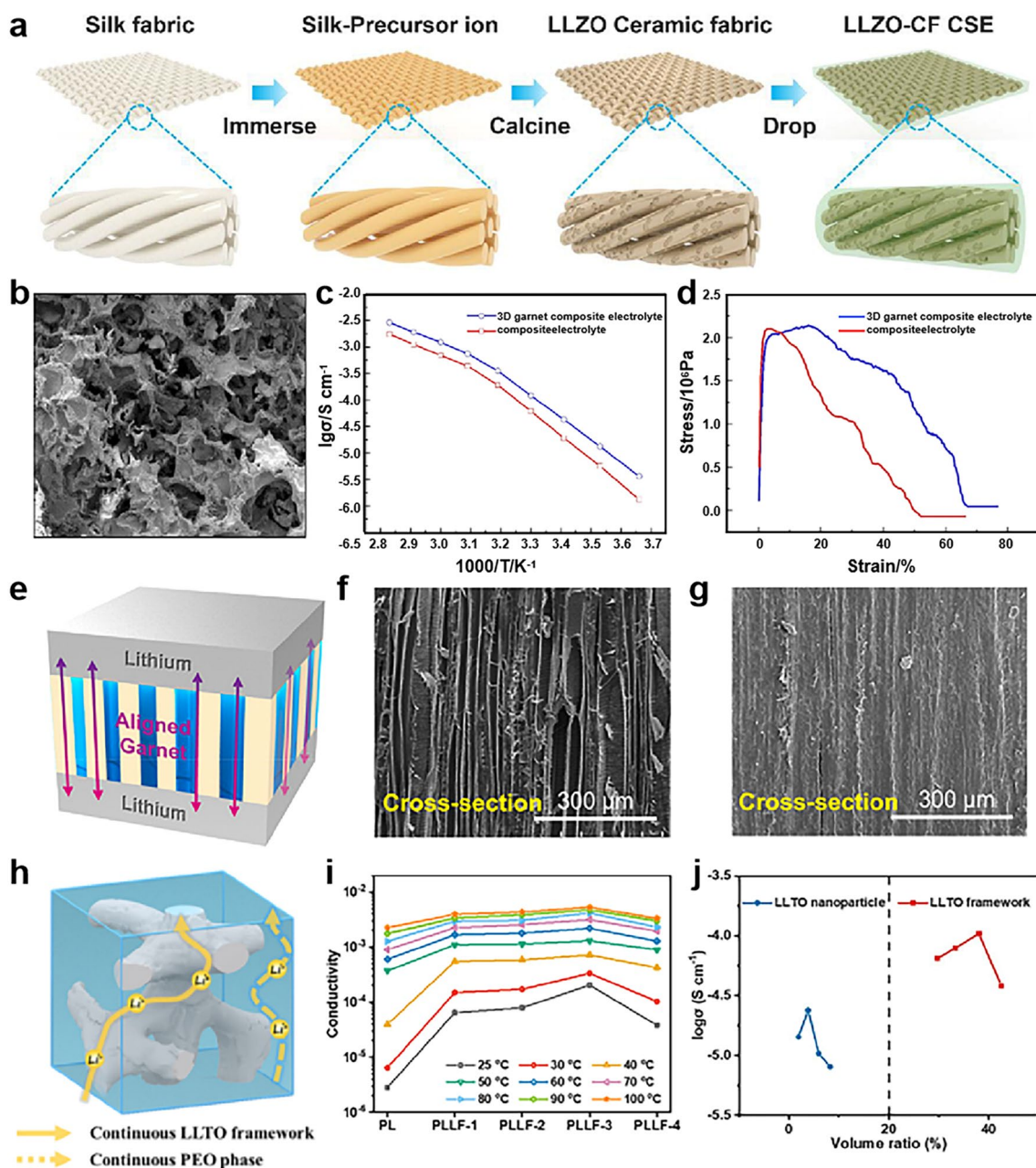


Fig. 4 **a** Schematic of the preparation of CSEs by the templating method. Reproduced with permission [127]. Copyright 2022, Elsevier. **b** SEM image of the garnet framework. **c** Arrhenius plots of the garnet/PEO CSEs. **d** Tensile test of the CSEs. **b–d** Reproduced with permission [101]. Copyright 2019, American Chemical Society. **e** Schematic of the Li symmetric cell with garnet-wood, showing the low tortuosity and fast lithium conduction pathways. SEM images of **f** pristine wood and **g** compressed wood. **e–g** Reproduced with permission [129]. Copyright 2019, American Chemical Society. **h** Schematic representation of possible Li^+ conduction pathway inside the PLLF electrolyte. **i** Ionic conductivity of PLLF electrolytes at different temperatures as a function of LLTO framework content. **j** The relationship between the volume ratio of inorganic components in the electrolyte and ionic conductivity at room temperature. **h–j** Reproduced with permission [133]. Copyright 2021, Elsevier

conduction pathways than the isolated ceramic phase in CSEs. For example, 3D continuous garnet/PEO CSEs templated by polymeric sponges exhibited higher ionic conductivity ($1.2 \times 10^{-4} \text{ S cm}^{-1}$) than isolated garnet particle/PEO

CSEs by the direct mixing of garnet particles and PEO–Li salt ($6.4 \times 10^{-5} \text{ S cm}^{-1}$) at 30°C (Fig. 4b, c). Meanwhile, the ion transference number (from 0.24 to 0.33), symmetrical cells (from 142 to 360 h), and mechanical strength

(elongation from 5% to 22%) were also improved (Fig. 4d) [101]. Second, the pore size of the template is also important for ionic conductivity. The structural regulation of the template can tailor the porous structure of ceramics to affect their performance. For example, different pore sizes of two nylon templates (0.2 and 0.4 μm) were used to prepare LLTO skeletons, and small pore size of 0.2 μm nylon template provides a higher porosity in the reversed LLTO replica than that using 0.4 μm nylon template [133]. It was found that high porosity effectively promotes the penetration of PEO matrix into the LLTO skeleton, which is conducive to CSE fabrication. Moreover, aligned pores of ceramics provide shortened ion conduction pathways (Fig. 4e). Thus, the ionic conductivity and electrochemical performance of the cell are greatly increased [84]. At present, aligned LLZO-based CSEs were prepared by a cylindrical shape microchannel wood template (Fig. 4f, g), which exhibited the highest Li^+ conductivity ($1.8 \times 10^{-4} \text{ S cm}^{-1}$ at 25 $^\circ\text{C}$) and broadened voltage window of 6.0 V [129]. However, there is currently no direct evidence comparing the advantages of aligned ceramic skeletons over twisted ones. Third, compared with ceramic in polymer CSEs (e.g., < 30 wt% ceramic fillers), 3D ceramic CSEs exhibit a higher percolation threshold, such as 70 wt% LLZTO [127], 63.3 wt% LAGP [126], 63 wt%

LLTO [133] and 50 wt% LLZO [128]. This is because the lower content of 3D ceramic will give rise to structural collapse upon removing the template, and sufficient 3D ceramic content could realize bicontinuous permeation networks for ion conduction. However, an excessively high content of ceramic framework with a reduced PEO phase will not be beneficial to the interfacial compatibility with the electrode, and there are also chances for the incomplete filling of PEO within 3D ceramic, failing to form continuous polymer ion channels. For example, Wang et al. [133] exhibited LLTO framework based CSEs (PLLF, Fig. 4h), which show the conductivity being the determination of mass ratios. As the mass ratio increased from 54 wt% (PLLF-1) to 63 wt% (PLLF-3), ionic conductivity increased from 6.45×10^{-5} to $2.04 \times 10^{-4} \text{ S cm}^{-1}$ (25 $^\circ\text{C}$). However, when the LLTO skeleton mass ratio achieved 67 wt% (PLLF-4), the ionic conductivity reduced slightly (Fig. 4i). The relationship between ionic conductivity and the volume ratio of the LLTO skeleton in the CSEs follows a similar trend at room temperature (Fig. 4j).

Currently, the majority of templates are naturally available and cost-effective. However, the precise tailoring of the template structure is restricted, which is not beneficial for performance. Therefore, it is necessary to design and

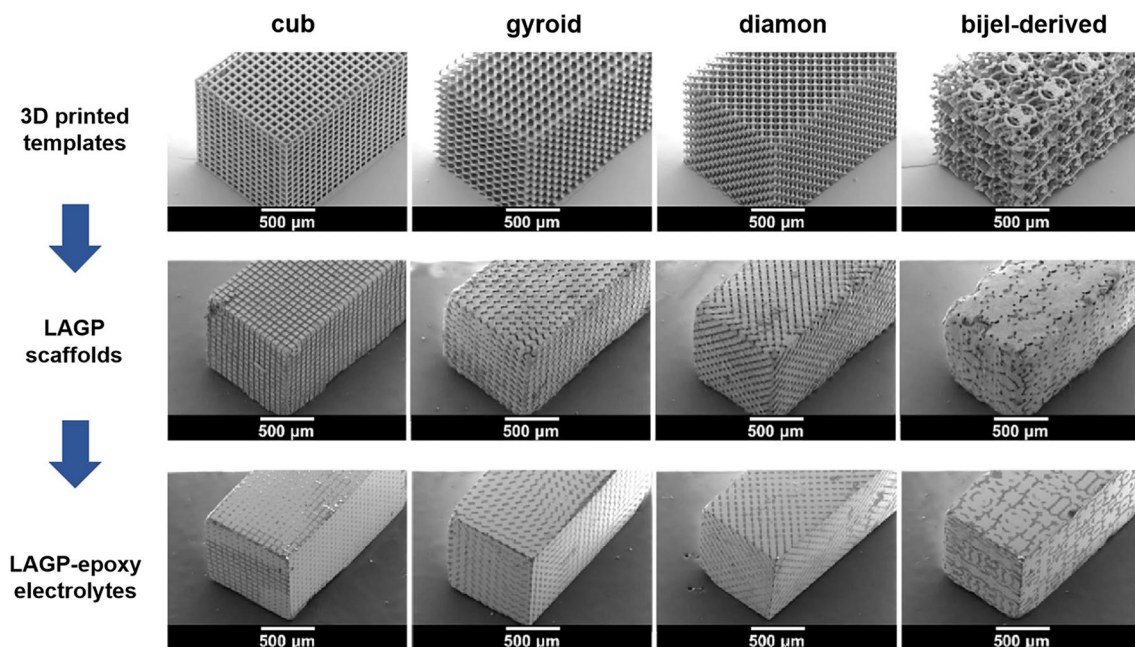


Fig. 5 SEM images of the 3D printed templates, the structured LAGP scaffolds and the structured LAGP-epoxy electrolytes with cube, gyroid, diamond and bijel-derived (left to right) microarchitectures. Reproduced with permission [134]. Copyright 2018, Royal Society of Chemistry

synthesize some special templates. In this case, 3D printed templates allow precise control over the ratio of ceramic-to-polymer and the microarchitecture. For example, Bruce et al. [134] prepared cube, gyroid, diamond and bijel-derived LAGP microarchitectures by 3D printing technology, which were filled with epoxy, delivering the best combination of mechanical strength and ionic conductivity (Fig. 5). The gyroid LAGP CSEs demonstrated an ionic conductivity of $1.6 \times 10^{-4} \text{ S cm}^{-1}$ at room temperature owing to decreased resistance at the grain boundaries of dense ceramic, and the

mechanical properties are as high as 28% of high compressive failure strain.

Various templating strategies are used to construct continuous ceramic skeletons to provide ion conduction channels, as summarized in Table 1. However, the thickness of CSEs is relatively high, which is unfavorable due to the transport distance [53, 135], such as 120 μm (polyurethane foam template) [101], 180 μm (cleanroom wiper template) [132] and 200 μm (cellulose textile template) [130]. Based upon the above, constructing a thin film with continuous, aligned and

Table 1 Performance comparison of electrolytes with different templates

Template	Composition	Thickness (μm)	LSV (V)	Ionic conductivity (S cm^{-1}) ($^{\circ}\text{C}$)	Ion transference numbers	Li symmetrical batteries	References
Silk	PEO–LiTFSI–70 wt% LLZO	127	5.1	8.89×10^{-5} (30)	0.49	Cycling with a current density of $100 \mu\text{A cm}^{-2}$ for 700 h at 50°C	[127]
Nylon	PEO–LiTFSI–63 wt% LLTO	120	4.7	2.04×10^{-4} (25)	0.59	Cycling from 0.1 to 0.4 mA cm^{-2} for 750 h at 60°C	[133]
Polyurethane foam	PEO–LiTFSI–40 wt% Ga–LLZO	200	5.6	1.2×10^{-4} (30)	0.33	Cycling with a current density of 0.4 mA cm^{-2} for 360 h at 60°C	[101]
Cotton	PEO–LiTFSI–50 wt% LLZO	200	5.5	0.89×10^{-4} (25)	0.27	Cycling with a current density of 0.5 mA cm^{-2} for 500 h at 25°C	[128]
Wood	PEO–LiTFSI–SCN–68 vol% LLZO	150	6	1.8×10^{-4} (25)	–	Cycling with a current density of 0.1 mA cm^{-2} for 180 h at room temperature	[129]
Cleanroom wiper	PEO–LiClO ₄ –20.7 wt% LLZAO	180	5.5	2.25×10^{-5} (30)	0.263	Cycling with a current density of 0.3 mA cm^{-2} for 100 h at 60°C	[132]
Ice	PEO–PEGDME–LiTFSI–63.3 wt% LAGP	100–200	–	1.67×10^{-4} (25)	0.56	Cycling from 0.1 to 0.3 mA cm^{-2} for 400 h at 60°C	[126]
Cellulose textile	PEO–LiTFSI–15 vol% LLZAO	200	–	6×10^{-5} (25)	–	Cycling from 0.05 to 0.2 mA cm^{-2} for 550 h at 60°C	[130]
3D print	Polypropylene–15 vol% LAGP	20	–	1.6×10^{-4} (25)	–	–	[134]
Bacterial cellulose	PEO–LiTFSI–40 wt% LLZO	70–100	6	1.12×10^{-4} (25)	–	–	[136]
Ice	PEO–LiClO ₄ –40 vol% LAMP	100	–	5.2×10^{-5} (25)	–	–	[137]
Polystyrene microspheres	PEO–LiTFSI–65.7 wt% LLZO	200	5.1	9.2×10^{-5} (25)	–	–	[131]

precisely controlled 3D ceramic CSEs is the goal of using the template strategy.

3.3 Electrospinning Approach

Different from mechanical mixing for ceramic in polymer and templating strategies for polymer in ceramic architectures, the electrospinning approach is suitable for preparing both ones. For the ceramic fillers in PEO CSEs, a polymer solution (e.g., PAN [53] and Polyimide [138]) was used as a precursor to form a freestanding porous substrate, and then PEO–Li salt was cast onto/into the above fibrous films. In this process, the ceramic fillers can be either incorporated into the electrospun polymer solution (e.g., PVDF [139]) or the PEO–Li salt solution. For the polymer in ceramic architecture, the preparation process is similar to the templating strategy with the electrospun polymer (e.g., polyvinyl pyrrolidone (PVP) [140] and polyvinyl alcohol (PVA) [141]) as a template for the formation of a freestanding porous ceramic framework via calcination, followed by the infiltration of PEO–Li salt solution.

The use of electrospun PAN film of the ceramic in polymer CSEs is beneficial to the stability with the cathode due to oxidation-resistant nitrile groups in PAN but is unfavorable for the ionic conductivity compared with PEO. For example, PAN films with PEO/LLZTO CSEs showed a higher electrochemical window of 4.7 V, superior to bare PEO/LLZTO CSEs (4.5 V). However, the ionic conductivity decreased from $8.18 \times 10^{-4} \text{ S cm}^{-1}$ (PEO/LLZTO CSEs) to $2.57 \times 10^{-4} \text{ S cm}^{-1}$ (PAN/PEO/LLZTO CSEs) [142]. The ionic conductivity can be tuned by the ceramic content in polymers with a percolation threshold [142–145]. For example, CSE with 20 wt% LLZO nanoparticles in electrospun PVDF films (denoted as 20-LLZO/h-polymer composite electrolyte) showed a maximum ionic conductivity of $1.05 \times 10^{-4} \text{ S cm}^{-1}$ at 50 °C (Fig. 6a–c) [139]. The polymer in ceramic CSEs was first reported by Hu et al. [146] in which a 3D LLZO ceramic network was prepared by electrospinning, followed by PEO–Li salt solution infiltration. Compared with the conventional templating strategy, it is found that the content of ceramic for forming 3D continuous networks is generally lower (10–40 wt% of total mass), such as 15 wt% LLZO [146] and 20 wt% LLTO [147]. We speculated that this might be due to the 1D fibrous networks formed by electrospinning.

The thickness of the above CSEs is related to the electrospun film thickness and the subsequent infiltration of PEO. For 3D ceramic CSEs, the thickness is reported in the range of 40–190 μm [140, 146, 148]. For example, a nanofiber network of PVP/LLTO film with a thickness of $\sim 60 \mu\text{m}$ was peeled off after spinning, and a final CSE thickness of 80–120 μm was obtained after calcination and PEO infiltration [147]. Designing much thinner CSEs is essential to achieve higher gravimetric and volumetric energy densities of full cells, which has become a current research hotspot. Interestingly, an ultrathin bilayer CSE of 4.2 μm (UFF/PEO/PAN/LiTFSI) was accomplished by filling the UFF porous scaffold (Fig. 6d) with a 1 μm PAN layer and a 3.2 μm PEO layer (Fig. 6e, f). In this design, a UFF film of 4.2 μm was prepared through the electrospinning of exfoliated vermiculite in the presence of PVA solution followed by heat treatment (Fig. 6d). The thickness of the UFF film was controlled by the electrospinning time. To fill the PEO layer, the UFF was placed on top of a viscous PEO film, which can automatically wet the UFF. After drying, the PAN solution was cast directly on the other side of the UFF film to obtain the resulting bilayer CSE. Benefiting from the bilayer polymer structure, the electrolyte achieved high compatibility with Li metal due to the PEO layer and an enlarged electrochemical window of 4.9 V due to PAN (Fig. 6g, h). Meanwhile, the stiff ceramic scaffold improves mechanical strength (Fig. 6i), delivering elastic moduli of 298 and 1072 MPa at the PEO and PAN sides, respectively, as measured by nanoindentation [141].

The macroscopic mechanical properties of ultrathin CSE films need to be cautiously considered for practical applications. There are also some thin porous polymer films in addition to electrospun polymers, such as polyimide [149, 150] and polyethylene films [135, 151], through which thin polymer solid electrolytes of $\sim 10 \mu\text{m}$ can be prepared by infiltration of PEO solution. However, CSEs also function as a separator. The thinner CSEs will inevitably reduce mechanical strength, and increase the risk of membrane fracture or Li dendrite penetration, resulting in internal short circuit, battery failure, and even potential safety hazards. Currently, most CSEs are $\sim 100 \mu\text{m}$ thick or more, and it remains a challenge to greatly reduce the thickness of CSEs without compromising their mechanical properties. Therefore, the relationship between the thickness and mechanical properties of CSEs needs to be systematically studied in the future.

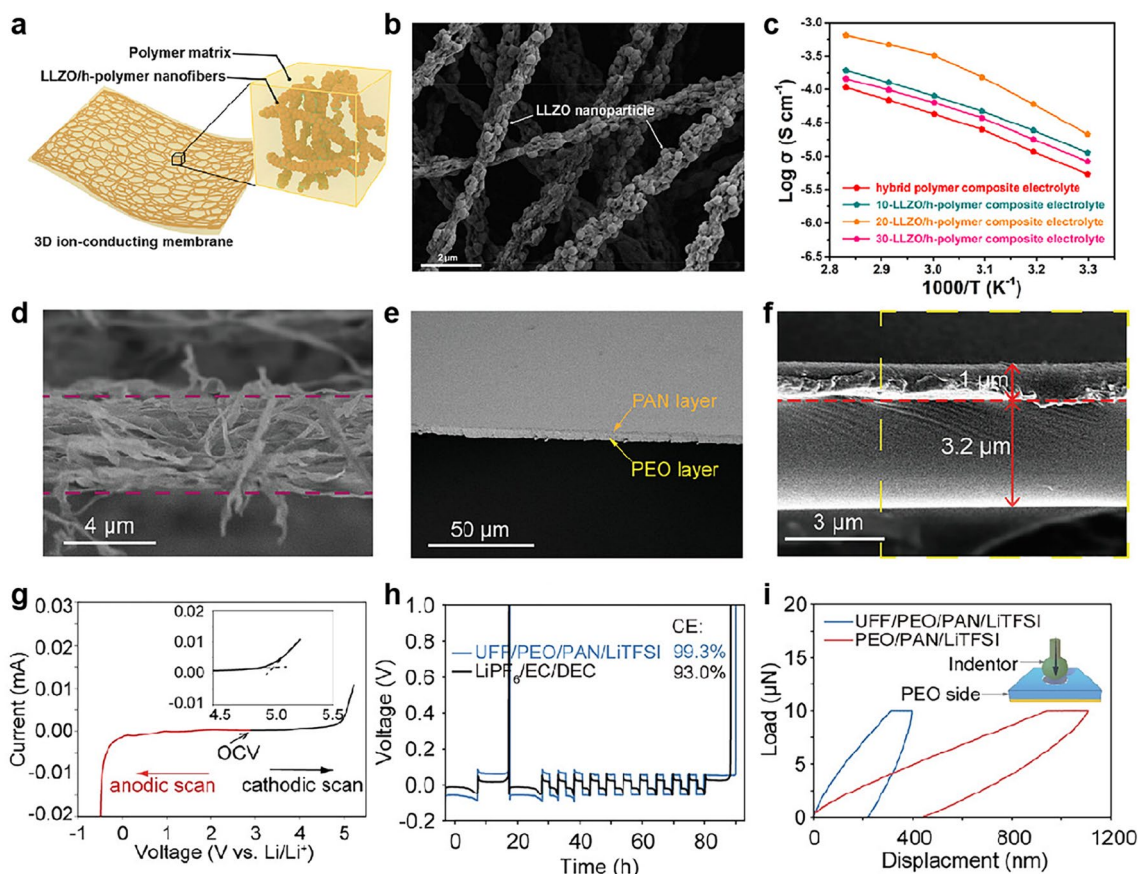


Fig. 6 **a** Schematic diagram of CSEs with LLZO/h-polymer nanofibers. **b** SEM image of 3D ion-conducting nanofiber networks. **c** Arrhenius curves of CSEs with polymer nanofibers and CSEs with LLZO-polymer nanofibers with different LLZO contents. **a–c** Reproduced with permission [139]. Copyright 2021, American Chemical Society. **d** Cross-sectional SEM image of the as-spun UFF. **e** Cross-sectional SEM image of the double-layer UFF/PEO/PAN/LiTFSI CSEs. **f** Cross-sectional SEM enlarged image of the UFF/PEO/PAN/LiTFSI CSEs. **g** The electrochemical window of the UFF/PEO/PAN/LiTFSI electrolyte. The inset is a magnified image of the onset of the oxidation process. OCV, open circuit voltage. **h** CE measurement of Li metal (known as Aurbach CE measurement) proposed by Aurbach in Li–Cu half cells using different electrolytes in Li–Cu half cells using different electrolytes. **i** Nanoindentation test on the PEO side of the UFF/PEO/PAN/LiTFSI and PEO/PAN/LiTFSI electrolytes. **d–i** Reproduced with permission [141]. Copyright 2021, Wiley–VCH

3.4 Gel Formation Approach

According to the process of gelatinization, the gel formation approach is divided into ceramic gels and polymer gels to obtain polymer in ceramic and ceramic in polymer architectures, respectively. For the ceramic gel-derived electrolytes, the hydrogel of the ceramic precursor is first prepared, followed by calcination to form a freestanding porous ceramic framework and finally PEO–Li salt solution infiltration. Polymer gel-based electrolytes can be readily prepared by one-pot polymerization of the monomer in the presence of ceramic fillers.

The concentrations of ceramic precursor salts, cross-linker and binder have an effect on the morphology of the ceramic gels and then the ionic conductivity. For example, by controlling the content of LLTO ceramic precursor salts and the crosslinker glutaraldehyde (Fig. 7a–d), the LLTO frameworks can exhibit nanoplate and dense particle morphology. More importantly, the binder amount can regulate the continuity of 3D ceramics with percolated structure both at the surface and inside of skeletons. When the content of binder PVA varied from 0.75 to 3.0 g (Fig. 7e–g), it was shown that 3.0 g PVA derived ceramic skeleton revealed a well-percolated structure (Fig. 7g). Correspondingly, the ionic conductivity increased to $8.8 \times 10^{-5} \text{ S cm}^{-1}$. However,

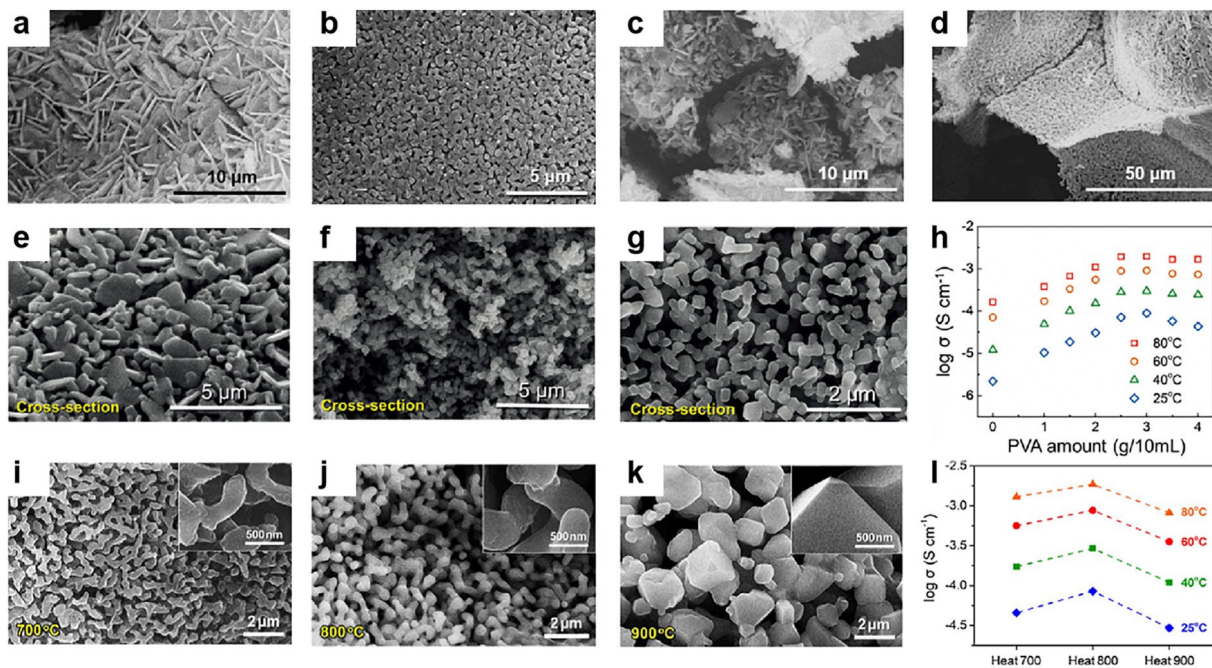


Fig. 7 SEM images of the LLTO framework with different LLTO amounts of **a, b** 1 mmol and **c, d** 3 mmol. The surface morphologies of LLTO frameworks after heat treatment at 800 °C with different amounts of PVA: **e** 0.75 g, **f** 1.5 g, and **g** 3.0 g. **h** The conductivity of LLTO CSEs with different PVA amounts from 0 (pure PEO) to 4 g. **a–h** Reproduced with permission [152]. Copyright 2018, Wiley–VCH. SEM images of 3D garnet frameworks heat treated at **i** 700 °C, **j** 800 °C, and **k** 900 °C for 2 h. The insets show high-magnification SEM images of 3D garnet frameworks. **l** Conductivity of 3D-CSEs with garnet frameworks heat treated at 700 °C (heat 700), 800 °C (heat 800) and 900 °C (heat 900). **i–l** Reproduced with permission [153]. Copyright 2018, Elsevier

when further increasing the PVA to 4 g, the ionic conductivity decreased slightly (Fig. 7h) [152]. Moreover, the morphology of the ceramic is also influenced by the heat treatment temperature. For example, the 3D garnet framework was thick branches porous, thicker branch porous and loosely connected microparticle structure when heating at 700, 800, and 900 °C, respectively (Fig. 7i–k). The results showed that the CSEs with optimized morphology and 3D interconnected structure (800 °C) exhibited the highest conductivity of $8.5 \times 10^{-5} \text{ S cm}^{-1}$ at room temperature (Fig. 7l) [153].

Polymer gel CSEs are essentially quasi-solid-state electrolytes, which are usually prepared by curing PEO monomer, Li-salt and ceramic fillers in the presence of photo/thermal initiator (e.g., benzophenone), as shown in Fig. 8a with ultraviolet irradiation (UV) polymerization. Firstly, cross-linked CSEs enable thermal stability even at relatively high temperatures due to polymer networks. For example, cross-linked CSEs exhibit well mechanical integrity after impedance test at 80 °C, avoiding short circuits of battery, while non-cross-linked CSEs lost

mechanical integrity (Fig. 8b) [154]. Secondly, ceramic fillers are used in CSEs to improve mechanical properties. All polymer gel CSE membranes with different content LATP (5, 10, 15 and 20 wt%) demonstrated the enhancement of tensile strength, compared with pure polymer gel electrolyte (Fig. 8c). Moreover, the type of ceramic conductor affects the ionic conductivity and electrochemical properties of gel electrolytes. For example, polymer gel-based CSEs with 10 wt% LATP showed a conductivity of $2.54 \times 10^{-4} \text{ S cm}^{-1}$ higher than that of polymer gel-based CSEs with 10 wt% LLTO ($2.81 \times 10^{-5} \text{ S cm}^{-1}$) at 25 °C. Interestingly, dual ceramic polymer gel-based CSEs with 10 wt% LATP and 15 wt% LLTO exhibited higher ionic conductivity of $9.87 \times 10^{-3} \text{ S cm}^{-1}$ at 25 °C, faster Li^+ transference number of 0.82 and wider electrochemical stability window of 5.43 V (Fig. 8d, e) as compared with a single ceramic gel based CSEs. This is because of UV cross-linked and well-dispersion of ceramic [155].

In addition, polymer gel electrolytes keep the merits of liquid electrolyte with high room temperature ionic conductivity ($\sim 10^{-3} \text{ S cm}^{-1}$) and Li^+ transport number (~ 0.8)

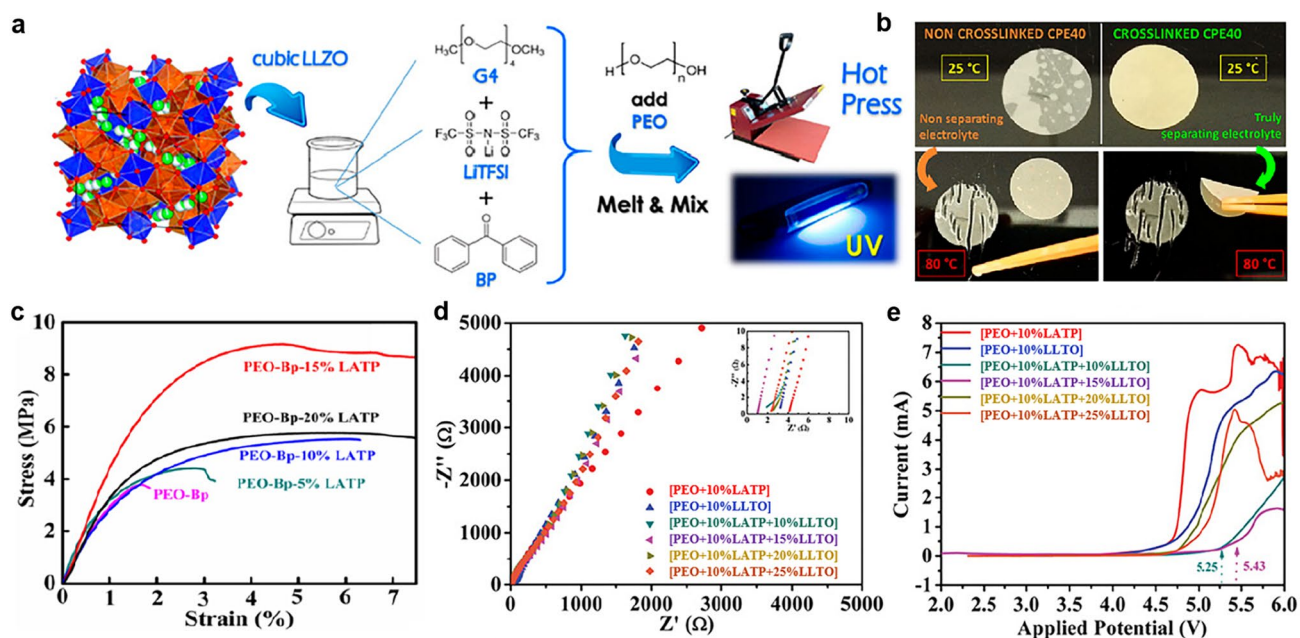


Fig. 8 **a** Schematic illustrations of the preparation process for CSE membranes via UV irradiation. **b** The difference in terms of mechanical integrity between non-cross-linked and cross-linked CSEs after impedance test at thermal stress. **a**, **b** Reproduced with permission [154]. Copyright 2019, American Chemical Society. **c** Stress–strain curves for PEO-Bp and PEO-Bp-LATP membranes. Reproduced with permission [156]. **d** Impedance-spectra and **e** linear sweep voltammetry (LSV) curves of polymer gel CSEs. **d–e** Reproduced with permission [155]. Copyright 2019, Elsevier

as well as endowing with improved safety and flexibility. Unfortunately, polymer gel CSEs absorb a large number of organic solvents easily leading to thermal runaway [156, 157]. More importantly, polymer gel CSEs have a higher thickness ($> 120 \mu\text{m}$), thus increasing the ion conduction distance, which is not conducive to the high energy density of solid-state batteries [151].

3.5 Other Approaches

In addition to the above well-established strategies, there are other useful and interesting strategies for the preparation of PEO/ceramic CSEs, which will be briefly covered in this section. For example, 3D porous ceramic skeletons were prepared by using pore-forming agents, e.g., SeS_2 [158] and graphite [38]. Moreover, high-temperature rapid reactive sintering can promote the surface diffusion of grains for neck growth and limit coarsening, accurately controlling the densification and the desired porous structure. 3D LLZTO porous scaffolds by rapid reactive sintering demonstrated good ionic conductivity ($\sim 1.9 \times 10^{-4} \text{ S cm}^{-1}$ at

room temperature) [159]. Furthermore, ultrathin CSE films were also fabricated by in situ polymerization with ceramic fillers on Li anodes. For example, a thin PEGMA/LAGP CSE of $8.5 \mu\text{m}$ was prepared by in situ copolymerization of PEGMEMA monomer in the presence of LAGP on a lithium anode, and the thickness of CSEs was controlled by scraping the mixed slurry, giving a prospective synergy of flexible-rigid property and interface compatible CSEs/lithium integration [160]. Likewise, other polymers can be also in situ polymerized in the presence of filler such as the ring-opening reaction of 1,3-dioxolane [161–163], polymerization of ethylene carbonate (EC) [164], and PEGMEA polymerization [38].

To summarize, the above preparation methods enable the design of a variety of polymer/ceramic CSE architectures with rapid progress. However, each of these methods has its strengths and limitations. One can combine concepts and tools from different strategies to develop CSEs with simultaneous high ionic conductivity and Li-ion transfer number, superior mechanical strength, flexibility and interfacial compatibility with the cathode/anode. In particular, the

interface compatibility both inside the CSEs (e.g., ceramic/polymer interfaces) and between CSEs/electrodes is critical to determine the performance, and thus, control over the interface compatibility is insightfully discussed in the following [165–168].

4 Interfacial Engineering

Surface modification of ceramic and constructing chemical bonds between ceramic/polymer are used for promoting smooth Li^+ transportation at ceramic/polymer interfaces to the same goal of solving the issue of ceramic/polymer interface compatibility. Meanwhile, the interface of CSEs/electrodes can also be specially designed according to the properties (such as reactivity under different potentials) of the cathode or anode.

4.1 Surface Modification of Ceramic

Introducing a coating layer on the surface of ceramic fillers is a promising strategy for increasing the interfacial compatibility of CSEs with ceramic in polymer architectures. The coating layer used includes polyethylene glycol (PEG) [35], polydopamine (PDA) [123] and ionic liquid [169], lithium polyacrylate [122], which can interact with ceramic via electrostatic adsorption or chemical bonding.

There are some criteria for the coating layer. First, the coating layer should have a similar surface energy to PEO for increasing the surface affinity between ceramic and polymer, greatly providing good compatibility and promoting Li^+ transportation at ceramic/polymer interfaces [94, 170]. For example, PDA-coated LLZTO showed a lower contact angle of 76° , whereas pristine LLZTO showed a higher contact angle of 116° with PEO solution (Fig. 9a). Thus, the CSEs with PDA@LLZTO fillers demonstrated a higher ionic conductivity of $1.15 \times 10^{-4} \text{ S cm}^{-1}$ than CSEs with bare LLZTO ($6.34 \times 10^{-5} \text{ S cm}^{-1}$) at 30°C (Fig. 9b) [123]. Similarly, ionic liquid ([BMIM]TF₂N) and PEG have also been used for coating ceramics, showing enhanced ionic conductivity [171]. Second, a suitable coating layer is necessary because an excess content of layers such as PEG or ionic liquid is detrimental to the mechanical properties [171]. For example, the CSEs with PEG showed a notable increase in ionic conductivity when elevating the PEG content. However, excessive PEG oligomer had a negative effect on the tensile strength of the membrane (Fig. 9c) [80]. Last but not least,

for some ceramic fillers with high electrical conductivity like MXene, the selection of a coating layer (generally electrical insulation) not only helps for dispersion but also could reduce the electrical conductivity of CSEs. This is because the high electrical conductivity of CSEs could give rise to dendrite formation [172]. For example, coating mesoporous silica nanosheets on MXene fillers can reduce the electrical conductivity from 1.4×10^3 to $2.3 \times 10^{-5} \text{ S cm}^{-1}$ [87].

The surface modification of ceramic can also alter the ion diffusion pathway from PEO to ceramic surfaces (Fig. 9d). A changed peak in the ^6Li NMR spectrum of molecular brush (MB)–LLZTO demonstrated that MB altered the Li^+ environment in the garnet (Fig. 9e). The quantified result of ^6Li spectrum of MB–LLZTO CSEs suggested more Li on the surface than in PEO and LLZTO lattices (Fig. 9f) [98]. Moreover, the modified ceramic can also reduce PEO crystallization and weaken the interaction between PEO and Li^+ as well as the interaction among various ions [35]. The introduced MB MB–LLZTO LLZTO reduced the crystalline area of the polymer, and further enhanced the ionic conductivity of CSEs ($3.11 \times 10^{-4} \text{ S cm}^{-1}$), which is higher than that of pristine LLZTO CSEs ($9.16 \times 10^{-5} \text{ S cm}^{-1}$) at 45°C (Fig. 9g) [98]. Furthermore, surface-functionalized ceramic particles can enlarge the Li^+ pathway in PEO chains, and the introduced anion can reduce the interaction between the polymer and Li^+ , thereby accelerating ion migration (Fig. 9h) [169]. For instance, grafting 1-methyl-3-trimethoxysilane imidazolium chloride (ILCl) to ZrO_2 , TiO_2 and SiO_2 were applied to CSEs. Compared with IL@ TiO_2 CSEs ($1.3 \times 10^{-4} \text{ S cm}^{-1}$) and IL@ SiO_2 CSEs ($7.15 \times 10^{-5} \text{ S cm}^{-1}$), the electrolyte with IL@ ZrO_2 displayed a higher ionic conductivity of $2.32 \times 10^{-4} \text{ S cm}^{-1}$ at 37°C owing to the stronger coordination of ZrO_2 nanoparticles and oxygen atoms in PEO chains (Fig. 9i) [169].

In addition, surface modification of the ceramic can also enhance the interface compatibility of the electrolyte/electrode, giving firmer binding and better contact. For instance, Li symmetric cells with PDA@LLZTO/PEO CSEs exhibited a lower interfacial resistance of $667 \Omega \text{ cm}^2$ than that of LLZTO/PEO CSEs ($1367 \Omega \text{ cm}^2$) at 20°C due to the surface transforming to super-lithiophilic after PDA coating [123]. Similarly, the CSEs composed of PEO and LLZTO modified with Si–R (3-glycidyloxypropyl)trimethoxysilane) layers also have decreased interfacial resistance by more than four magnitudes [173]. Various modified ceramics were used for CSEs that not only exhibit higher ionic conductivity and

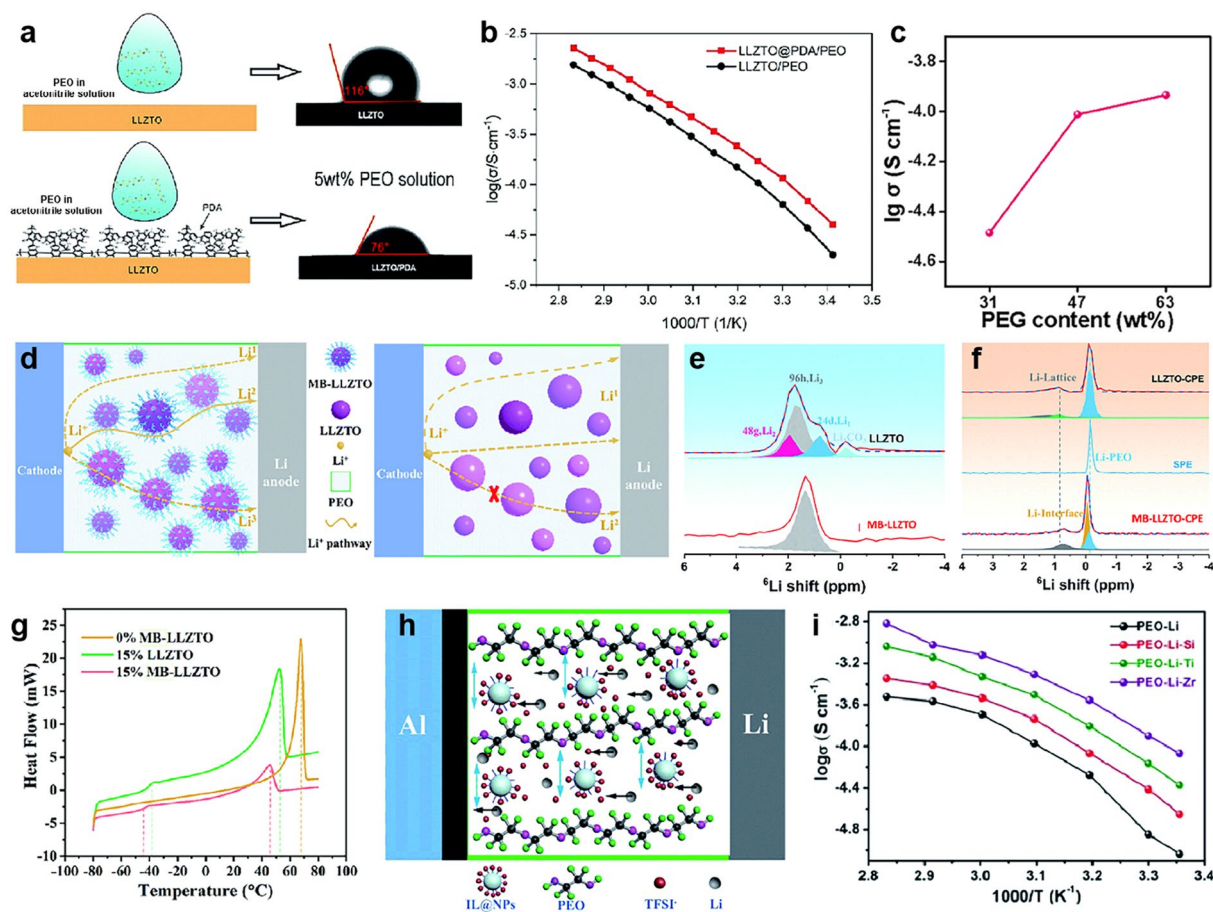


Fig. 9 **a** Schematic of dopamine polymerized on the surface of LLZTO particles to form a polydopamine coating layer and contact angle between the PEO solution (dissolved in acetonitrile) and pristine LLZTO or LLZTO@PDA. **b** Arrhenius plots of PEO/LLZTO@PDA and PEO/LLZTO CSEs. **a, b** Reproduced with permission [123]. Copyright 2019, Royal Society of Chemistry. **c** Ionic conductivity of electrolyte membranes with different PEG contents. Reproduced with permission [80]. Copyright 2022, Elsevier. **d** Diagrams of the Li⁺ diffusion pathway in the MB-LLZTO CSEs and LLZTO CSEs. **e** ⁶Li NMR of LLZTO and MB-LLZTO materials. **f** ⁶Li direct polarization NMR spectra and assignment results for the LLZTO and MB-LLZTO CSEs. The blue area represents Li in PEO, the orange area represents the interfacial Li, and the gray and green areas correspond to the LLZTO lattice in **e, g** DSC thermograms of electrolytes with different coating layers. **d–g** Reproduced with permission [98]. Copyright 2019, Royal Society of Chemistry. **h** Schematic illustration of ionic liquid grafted oxide nanoparticles (IL@NPs). **i** The ionic conductivity of CSEs with different IL@NP fillers at different temperatures. **h–i** Reproduced with permission [169]. Copyright 2017, Royal Society of Chemistry. (Color figure online)

lower interfacial resistance but also possess a wider electrochemical stability window and better tensile strength, as illustrated in Table 2. However, systematic investigation on the type and thickness of the modified layer is still lacking, and future endeavors are suggested to optimize the performance.

4.2 Constructing Chemical Bonds

In addition to the above-mentioned surface coating, theoretically speaking, constructing chemical bonds can not

only ensure the uniform dispersion of ceramic in CSEs for improving ionic conductivity but also increase the mechanical strength of CSEs by using ceramic as a crosslinker [174]. The in situ chemical grafting is frequently used to construct chemical bonding between ceramic fillers and polymer matrix, including in situ hydrolysis [175–178], ring-opening reactions [97], silane coupling [179] and vapor phase infiltration (VPI) chemical incorporation [180], for forming an interpenetrating polymer-ceramic network, providing dense and uniform interface Li⁺ transport channels, as seen in Fig. 10a with the intermolecular interaction of EC and LLZTO in PEO [97].

Table 2 Performance comparison of electrolytes with different surface modifiers

Modifier	Composition	Ionic conductivity (S cm^{-1}) ($^{\circ}\text{C}$)	LSV (V)	Li symmetrical batteries	References
Mesoporous SiO_2	PPO-LiTFSI-2 wt% Ti_3C_2	7×10^{-10} (25)	–	–	[87]
	PPO-LiTFSI-2 wt% Ti_3C_2 @m SiO_2	4.6×10^{-4} (25)	4.3	Cycling with a current density of 0.2 mA cm^{-2} for 500 h at room temperature	
PDA	PPO-LiTFSI-80 wt% LLZTO	6.34×10^{-5} (30)	4.5	Cycling with a current density of 0.2 mA cm^{-2} for 78 h at $50 \text{ }^{\circ}\text{C}$	[123]
	PPO-LiTFSI-80 wt% LLZTO@PDA	1.15×10^{-4} (30)	4.8	Cycling with a current density of 0.2 mA cm^{-2} for 400 h at $50 \text{ }^{\circ}\text{C}$	
IL	PEO-LiTFSI-20 wt% ZrO_2	1×10^{-4} (70)	–	–	[169]
	PEO-LiTFSI-20 wt% ZrO_2 @IL	2.32×10^{-4} (37)	4.9	–	
HBPAE	PEO-7.5 wt% TiO_2	–	–	–	[94]
	PEO-15 wt% TiO_2 @HBPAE	3.2×10^{-3} (35)	–	–	
Si-R	PEO-LiTFSI-30 wt% LZTO	1×10^{-3} (–)	–	–	[173]
	PEO-LiTFSI-30 wt% LLZTO@P	5×10^{-3} (–)	–	–	
	PEO-LiTFSI-30 wt% LLZTO@P + Si-R	9×10^{-3} (–)	–	–	
IL	PEO-LiTFSI-15 vol% LLZTO	1.7×10^{-5} (20)	4.6	–	[171]
	PEO-LiTFSI-15 vol% LLZTO@IL	2.2×10^{-4} (20)	4.85	Cycling with a current density of 0.5 mA cm^{-2} for 7500 h at $30 \text{ }^{\circ}\text{C}$	
MB	PEO-LiTFSI-LLZTO	–	–	–	[98]
	PEO-LiTFSI-15 wt% LLZTO@MB	3.11×10^{-4} (45)	4.5	–	

Ceramic particles uniformly disperse in CSEs by in situ hydrolysis of ceramic precursors, further lowering the crystallinity of PEO. For example, the crystallinity of in situ SiO_2 based CSE is 19.1%, while the crystallinity of ex situ SiO_2 CSE prepared by mechanical mixing is 20%. Correspondingly, the endothermic peak of ex situ SiO_2 CSE appears at $49.9 \text{ }^{\circ}\text{C}$, higher than that of in situ SiO_2 CSE ($43.8 \text{ }^{\circ}\text{C}$). The in situ SiO_2 -based CSE had improved ionic conductivity of $1.8 \times 10^{-4} \text{ S cm}^{-1}$ as compared with ex situ SiO_2 CSE ($7.9 \times 10^{-5} \text{ S cm}^{-1}$) at room temperature [76]. Benefiting from lower crystallinity of VPI-ZnO CSE at relatively low temperatures ($< 50 \text{ }^{\circ}\text{C}$), VPI-ZnO CSE possessed higher ionic conductivity of $1.5 \times 10^{-5} \text{ S cm}^{-1}$ at $25 \text{ }^{\circ}\text{C}$, compared with physical mixing (PM)-ZnO CSEs (Fig. 10b). Nevertheless, the ionic conductivity of VPI-ZnO CSEs was only marginally improved (Fig. 10b) due to the similar crystallinities of two samples at a temperature of nearing or higher than the melting points of PEO (Fig. 10c) [180]. Moreover, the modified PEO/ceramic interface ensures a fast Li^+ conduction channel and reduces Li^+ accumulation on the interface of the electrode/electrolyte, thus regulating Li^+ deposition at the lithium anode [97]. For example, Li symmetry batteries with VPI-ZnO CSEs exhibited a low

voltage polarization of approximately 40 mV, and the cycle life of the battery was prolonged to 450 h. While the symmetry batteries with PM-ZnO CSEs showed an increased overpotential to $\sim 70 \text{ mV}$, only extending the cycle life to 284 h (Fig. 10d) [180]. Not only that, but electrochemical stability also greatly improved. For example, the coupled-LGPS CSEs start to decompose at about 5.1 V, while the mixed-LGPS CSE is approximately 4.8 V (Fig. 10e) [179].

More importantly, the mechanical strength of CSEs greatly improved due to form an interconnected network, which could effectively inhibit the growth of lithium dendrites (Fig. 10f). For example, the CSEs composed of 2D boron nitride nanosheets (BNNs) and poly(ethylene glycol)diacrylate (PEGDA) by coupled using a silane coupling agent and exhibited an ultrahigh mechanical strength ($> 26.2 \text{ MPa}$), higher than that of uncoupled BNN CSEs (4.70 MPa , Fig. 10g). The Li symmetrical cells with coupled-BNNs also presented more uniform lithium plating/stripping, and lower overpotentials (Fig. 10h) [86]. Moreover, organic crosslinkers affect mechanical properties of CSEs. For example, the elongation and tensile strength of PEO/LiTFSI/EC CSEs decreased with adding EC, but greatly increased with adding LLZTO particles.

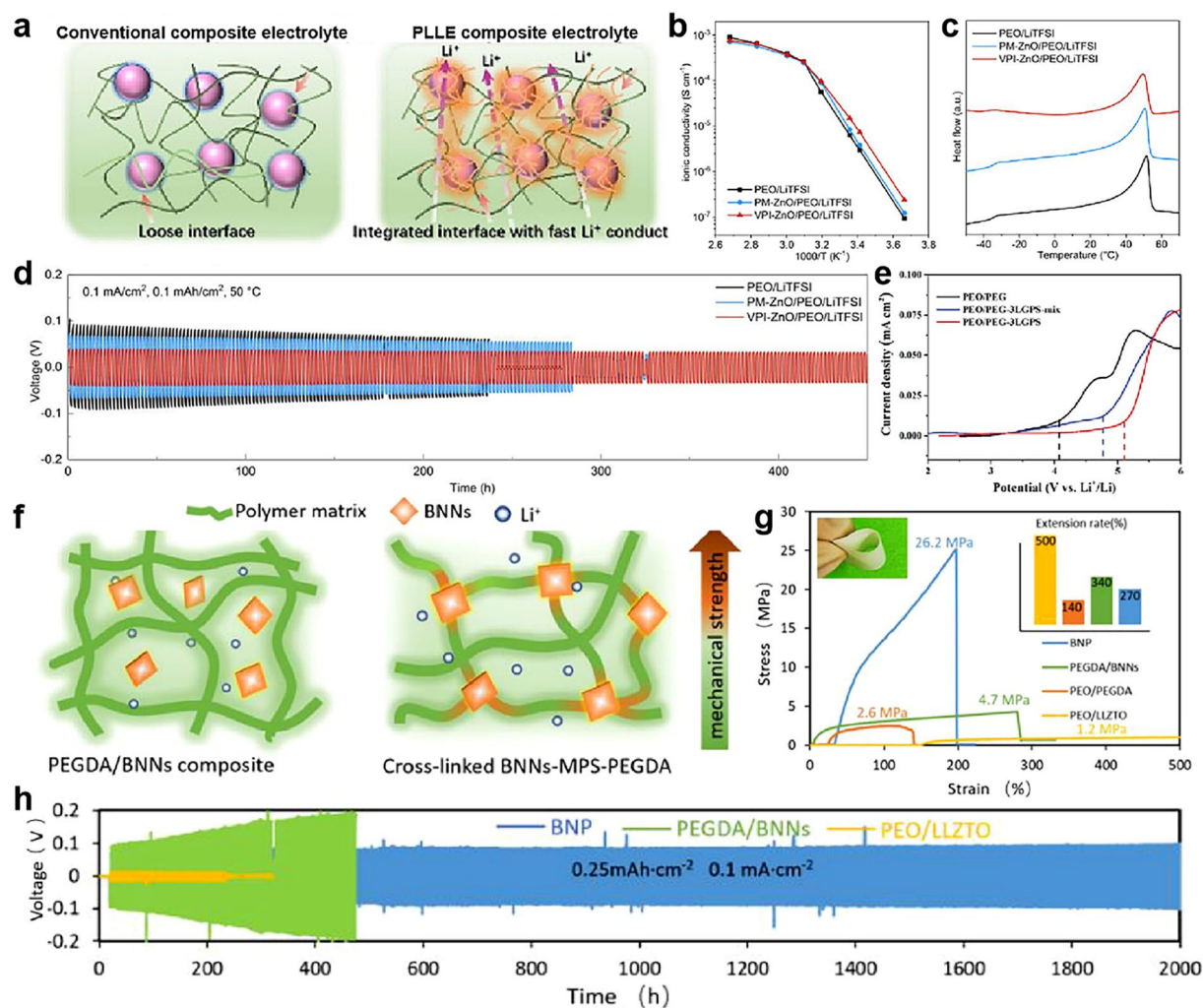


Fig. 10 **a** Schematic figures of the synergistic effect of the components in CSEs. Reproduced with permission [97]. Copyright 2021, Wiley-VCH. **b** The relationship between ionic conductivity and temperature for each electrolyte. **c** DSC profiles of each electrolyte. **d** Long-term galvanostatic cycling of Li–Li symmetric cells. **b–d** Reproduced with permission [180]. Copyright 2021, Elsevier. **e** LSV curves of each electrolyte at room temperature. Reproduced with permission [179]. Copyright 2020, Wiley-VCH. **f** Schematic diagram of the structure of PEGDA/BNNs and BNP. **g** Stress–strain curves of different polymer electrolytes. **h** Long-cycle performance of Li symmetrical cells. **f–h** Reproduced with permission [86]. Copyright 2021, Elsevier

Interestingly, the CSEs composed of PEO and LLZTO via ring-opening reaction of EC exhibited the best ionic conductivity of $1.43 \times 10^{-3} \text{ S cm}^{-1}$ at 25 °C, which is approximately equal to the ionic conductivity of a commercial liquid electrolyte ($10^{-3} \sim 10^{-2} \text{ S cm}^{-1}$ at room temperature). However, the thickness of the electrolyte is not mentioned [97].

The CSEs improved interface compatibility between polymer and ceramic by constructing chemical bonds, thus increasing ionic conductivity and mechanical properties, extending the long-cycle performance of Li symmetrical cells.

4.3 Interface Optimization of Electrode/CSEs

Surface modification and constructing chemical bonds are utilized to resolve the issue of interface incompatibility of polymer/ceramic, and the ionic conductivity has been greatly improved, which is no longer the main bottleneck for the development of CSEs. Currently, the greatest challenge comes from the incomplete contact interface of the electrode/electrolyte that will prevent Li⁺ transport through the interface and only from the point-to-point intimate contact sites, resulting in high interface resistance [181, 182]. The

large interfacial resistance leads to a slow Li^+ transmission rate and uneven current distribution during battery operation. Moreover, volumetric changes of active materials and side reactions caused by the incompatibility of the electrolyte/electrode during battery operation also severely limit their performance [183].

The superb interface can enable low interfacial resistance and efficient Li^+ transport, thus significantly improving battery performance. Thus, the rational design of high stability CSEs is significantly important. Changing the structure of CSEs significantly reduces interface impedance and provides more Li^+ transport contact sites [184, 185]. For example, changing structure of PEO/garnet electrolyte forms a sandwich structure of PEO/LLZO/PEO [181]. For ceramic embedded CSEs, some hard-to-hard contact still exists originating from the exposed ceramic surface in CSEs. Incorporating a PEO layer on either side of PEO/LLTO CSEs prevented direct contact between LLTO and electrodes (Fig. 11a). From SEM images of PEO/LLTO CSEs with two PEO layers, PEO–LiTFSI was partially immersed into LiFePO_4 cathode and achieved a tight interface contact (Fig. 11b). In contrast, the poor interface of the CSEs without being covered by the PEO layer and LiFePO_4 cathode led to worse performance and an obvious gap between the LiFePO_4 cathode and CSEs is clear (Fig. 11c) [183].

Moreover, to further improve interface contact between electrolyte and electrode, introducing an extra surface modification layer on the surface of CSEs or electrode (e.g., adaptive buffer layer (ABL) [186] and Li phosphorous oxynitride (LIPON) [187]) is adopted to form CSEs for better electrochemical performance in usage for application. For example, introducing an ABL on the surface of CSE (Fig. 11d) and the battery had a small change in total resistance (increase of 6%–14%, Fig. 11e). In contrast, the total resistance increased from 43% to 63% (Fig. 11f) after cycling without ABL. This shows that the ABL can effectively prevent the decrease of the overall ionic conductivity during cycling [186]. In addition, the modification can also be on the Li anode such as LIPON-modified Li anode, to improve the compatibility between PEO/LAGP CSEs and Li anode in solid-state batteries, which offered an evenly Li^+ flux and effectively inhibited Li dendrite formation in solid-state batteries [187].

To improve the chemical compatibility of CSEs with high-voltage cathodes, an antioxidant polymer (e.g., PAN) is introduced to enlarge the electrochemical window of CSEs (Fig. 11g) [188, 189]. For example, a bilayer CSE

with PAN/PEO/UFF showed improved electrochemical stability (4.9 V), compared with PEO/UFF electrolyte without a PAN layer (4.1 V) [141]. In addition, the PAN fiber networks endow PEO/LLZTO CSEs with high oxidation resistivity, accordingly an electrochemical stability window as high as 4.7 V (Fig. 11h), higher than that of the CSEs without PAN (4.5 V, Fig. 11i) [142].

The design of CSEs improved solid–solid interface compatibility, thus maintaining better interfacial contact during battery cycling, promoting the practical application of solid-state batteries. Meanwhile, the failure process of CSEs and lithium metal deposition can be visualized by multiphysics simulation [190, 191]. Therefore, the interface optimization approach combined with multiphysics simulation has promising prospects for the rational design and development of safe solid-state batteries.

5 Applications of PEO/Ceramic CSEs

Based on the advantage of PEO/ceramic CSEs, such as enhanced ionic conductivity, optimized interfacial contact, high mechanical tolerance, and excellent chemical and electrochemical stability, the PEO/ceramic CSEs coupled with anode and cathode are expected to achieve high energy density and safety solid-state batteries. This section will mainly discuss the application of PEO/ceramic CSEs in solid-state lithium metal batteries (SSLMB) with transition metal oxides and sulfur cathodes.

5.1 SSLMB with Transition Metal Oxides Cathode

Solid-state electrolytes are a pivotal part of solid-state battery, which determines the energy and power density, cycle stability, safety performance and service life to a large extent. Some PEO/ceramic CSEs have been reported with high ionic conductivity ($10^{-4} \sim 10^{-3} \text{ S cm}^{-1}$ at room temperature), especially for polymer gel-based CSEs, which is no longer the most main problem for the practical application of solid-state batteries [99, 114, 192]. However, solid–solid interface contacts between electrodes and electrolytes, unlike the wettable liquid electrolyte, will seriously affect Li^+ transport, increasing internal resistance, and thus deteriorating the cycle and rate performance of battery. Besides, coupled cathode materials currently used are LiFePO_4 (LFP, <4 V), LiCoO_2 (LCO, ~ 4.3 V) and $\text{LiNi}_x\text{Mn}_y\text{Co}_z\text{O}_2$

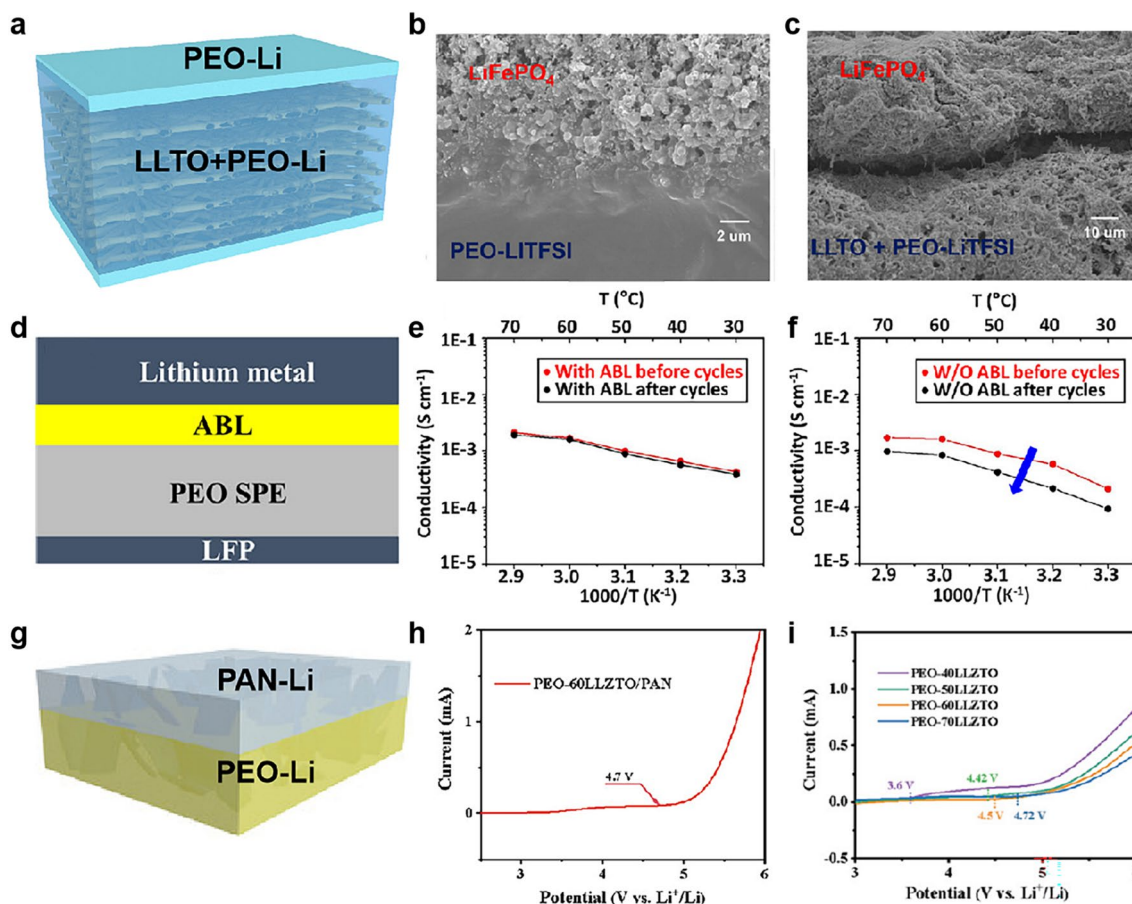


Fig. 11 **a** Schematic of the PEO/PEO–LLTO/PEO CSEs. **b** Cross-sectional SEM images of the PEO–LiTFSI–LLTO//LiFePO₄ and **c** PEO–LiTFSI–LLTO–O//LiFePO₄ interfaces. **a–c** Reproduced with permission [183]. Copyright 2019, American Chemical Society. **d** Schematic of the interface contact between the Li metal anode and electrolyte with the ABL. Arrhenius plots of the conductivities of full batteries. **e** Li/ABL/electrolyte//LiFePO₄ and **f** Li/electrolyte//LiFePO₄ before and after 150 cycles. **d–f** Reproduced with permission [186]. Copyright 2019, American Chemical Society. **g** Structural characterization of the bilayer UFF/PEO/PAN/LiTFSI. Reproduced with permission [141]. Copyright 2021, Wiley–VCH. **h** LSV profile of CSEs with PAN. **i** LSV profiles of CSEs with different contents of LLZTO (without PAN). **h, i** Reproduced with permission [142]. Copyright 2021, Wiley–VCH

(NMC, ~4.3 V). Among those, LFP is extensively matched with PEO/ceramic CSEs due to lower potential (< 4 V), as illustrated in Table 3. However, used CSEs were limited in their potential for high-voltage applications due to the narrow electrochemical window of PEO (~3.9 V) [193]. In addition, some factors, such as, the thickness of CSEs, the mass of lithium metal anode, the areal capacity in cathode, negative/positive capacity (N/P) ratio, are highly regarded for realizing high-energy–density solid-state lithium metal batteries.

First, better interface compatibility between electrodes and electrolytes is conducive to interface Li⁺ transport, improving cycle and rate performance of battery, which

includes the interface of electrolytes/lithium anode and electrolytes/cathode. As shown in Sect. 4.3, changing the structure of hard-to-hard contact to soft-to-hard contact or introducing an extra surface modification layer can mitigate the incomplete contact interface, providing more Li⁺ transport contact sites. Meanwhile, increasing the contact area can enhance interface compatibility by constructing composite cathodes composed of the electrolyte and cathode materials [46, 53, 139]. Second, the greater the potential difference between the positive and negative electrodes, the higher the working voltage, and the higher the energy density of battery. Thus, enlarging the electrochemical stability window of CSEs to or more than 4.3 V is essential for assembling with

Table 3 Performance comparison of various lithium metal batteries with PEO/ceramic CSEs

Cell composition	Active materials (mg cm ⁻²)	Current density (mA g ⁻¹)	Temperature (°C)	Specific capacity (mAh g ⁻¹)	Areal capacity (mAh cm ⁻²)	Cycle number	References
LFP/PEGMA–LiTFSI–LAGP/Li	1	85	30	123	0.123	300	[160]
LCO/PEGMA–LiTFSI–LAGP/Li	1	274	60	140.4	0.140	120	
LFP/PEO–LiTFSI–LLZTO/Li	0.8	100	60	136.4	0.109	850	[80]
LFP/PEO–LiTFSI–LLZO/Li	1.5	34	50	149.3	0.224	100	[127]
LFP/PEO–LiTFSI–LATP–PE/Li	1.5	170	20	93	0.140	1000	[39]
LFP/PEO–LiTFSI–LLZTO/Li	1.2	34	40	116.9	0.140	500	[194]
LFP/PEO–LiTFSI–LLZAO/Li	1.1	17	60	160	0.176	200	[89]
NCM/PEO–LiTFSI–LLZAO/Li	1.1	17	60	150	0.165	50	
LFP/PEO–LiTFSI–Mg(ClO ₄) ₂ /Li	5	20	55	157	0.785	–	[46]
NCM811/PEO–LiTFSI–Mg(ClO ₄) ₂ /Li	3	33	55	145	0.435	–	
LFP/PEO–LiTFSI–LLZO/Li	3.1	34	60	151.7	0.470	500	[28]
NCM622/PEO–LiTFSI–LLZO/Li	3.1	56.2	60	145.3	0.450	200	
LFP/PEO–PVDF–LiTFSI–LLZO /Li	1.5	34	50	148.8	0.223	180	[139]
LFP/PEO–LiTFSI–LLTO/Li	1	17	60	154.7	0.155	150	[133]
NCM523/PEO–LiTFSI–LLTO/Li	2	141	60	137.2	0.274	100	
NCM622/PEO–PAN–LiTFSI–UFF/Li	23	13	50	163	3.749	100	[141]
f-Al ₂ O ₃ @NCM523/PEO–PVDF–LiTFSI–LLZTO–OX/Li	2	27.2	55	150.6	0.301	80	[124]
NCM811/PEO–LiTFSI–VPI–ZnO/Li	1.75	140	50	164.7	0.288	200	[180]
LFP/PEO–PEGDA–LiTFSI–BNNs/Li	6.4	34	25	140	0.896	150	[86]
LFP/PEO–LiCF ₃ SO ₃ –LATP/Li	5	85	60	118.2	0.591	1000	[92]
LFP/PEO–LiClO ₄ –SiO ₂ /Li	1	34	55	123.5	0.124	100	[178]
LFP/MXene–mSiO ₂ /ePPO/Li	2	85	25	141.8	0.284	250	[87]
LFP/PEO–LiTFSI–SN–SiO ₂ /Li	2.52	85	60	159.5	0.402	70	[195]
LFP/PEO–LiTFSI–MnO/Li	1.3	85	60	143.5	0.187	300	[90]
LCO/PEO–LiTFSI–MnO/Li	4.3	27.4	25	122.4	0.526	1000	[196]
NCM622/PEO–LiTFSI–LLZTO–SN/Li	4.8	140.5	25	153.4	0.736	300	
LFP/PEO–LiTFSI–LLZTO/Li	1	17	60	153.7	0.154	200	[120]
LFP/PEO–LiTFSI–LLZO/Li	1.68	85	60	158.8	0.267	70	[117]

a high voltage cathode. Introducing high oxidation-resistant ceramics (Li⁺-insulate and Li⁺ Li⁺-conduct) or organic additives (e.g., PAN, SN) is feasible. For example, casting PEO/LiTFSI/LLZTO/SN onto PAN fiber network CSEs exhibited an increased electrochemical stability window from 3.6 (PEO/LiTFSI) to 4.72 V due to the participation of SN, PAN and LLZTO [142]. As mentioned above, surface modification of ceramics and constructing chemical bonds can also further improve the electrochemical stability of CSEs. For example, graft-coupled BNNs with PEGDA CSEs exhibited a stable electrochemical window of 5.5 V, which is higher than that of the uncoupled BNNs CSE (5.0 V) [86].

In addition, benefiting from increasing active materials loading in cathode, the higher areal capacity furtherly enables energy density of batteries [151]. However, the excess high load will lead to failure in operating of the battery at a higher current density. For example, LFP//Li full cells with PEO/PEGDA/LiTFSI/BNNs CSEs exhibited a capacity of 0.25 mAh cm⁻² at 0.5 C under load of 2 mg cm⁻², when the load increased to 8 mg cm⁻², the cell can't operate at 0.5 C, but showed an enhanced capacity of 1.05 mAh cm⁻² at 0.2 C [86]. Meanwhile, the full cells demonstrate better capacity at a higher test temperature (> melt temperature) due to the lower crystallinity of PEO. For example, under a current

density of 0.5 C, LFP//Li full cells with PEGMA/LiTFSI/LAGP CSEs displayed capacities of 0.123 and 0.151 mAh cm⁻² at 30 and 60 °C, respectively [160]. At present, the vast majority of full cells with PEO/ceramic CSEs exhibit an areal capacity of <1.1 mAh cm⁻² (Fig. 12a, b) and operate long cycles at only higher temperatures (Fig. 12c, d). Especially, the NCM811//Li full cell with a bilayer CSE composed of PAN/UFF/PEO delivered a high capacity of 3.6 mAh cm⁻² at 0.1 C and 50 °C due to superior active material load (17–20 mg cm⁻²), which reaches a level of commercialization (3.5 mAh cm⁻²). However, the full cell

showed an uneventful cycle number of 150 and a lower capacity retention of 67% [141]. At present, the great majority of SSLMB with PEO/ceramic CSEs display a higher N/P ratio (> 100) due to the difficulty in achieving ultrathin lithium anode lower than 50 μm. Fortunately, an ultrathin lithium foil of 35 μm was coupled with NCM811 cathode (10.3 mg cm⁻²) in the presence of plastic-crystal-embedded elastomer CSEs (25 μm), and the cell displayed a lower N/P ratio of 3.4, a higher energy density of 410 Wh kg⁻¹, which is one of the record values among SSLMB based on PEO-based CSEs, to the best of our knowledge (Table 3) [50].

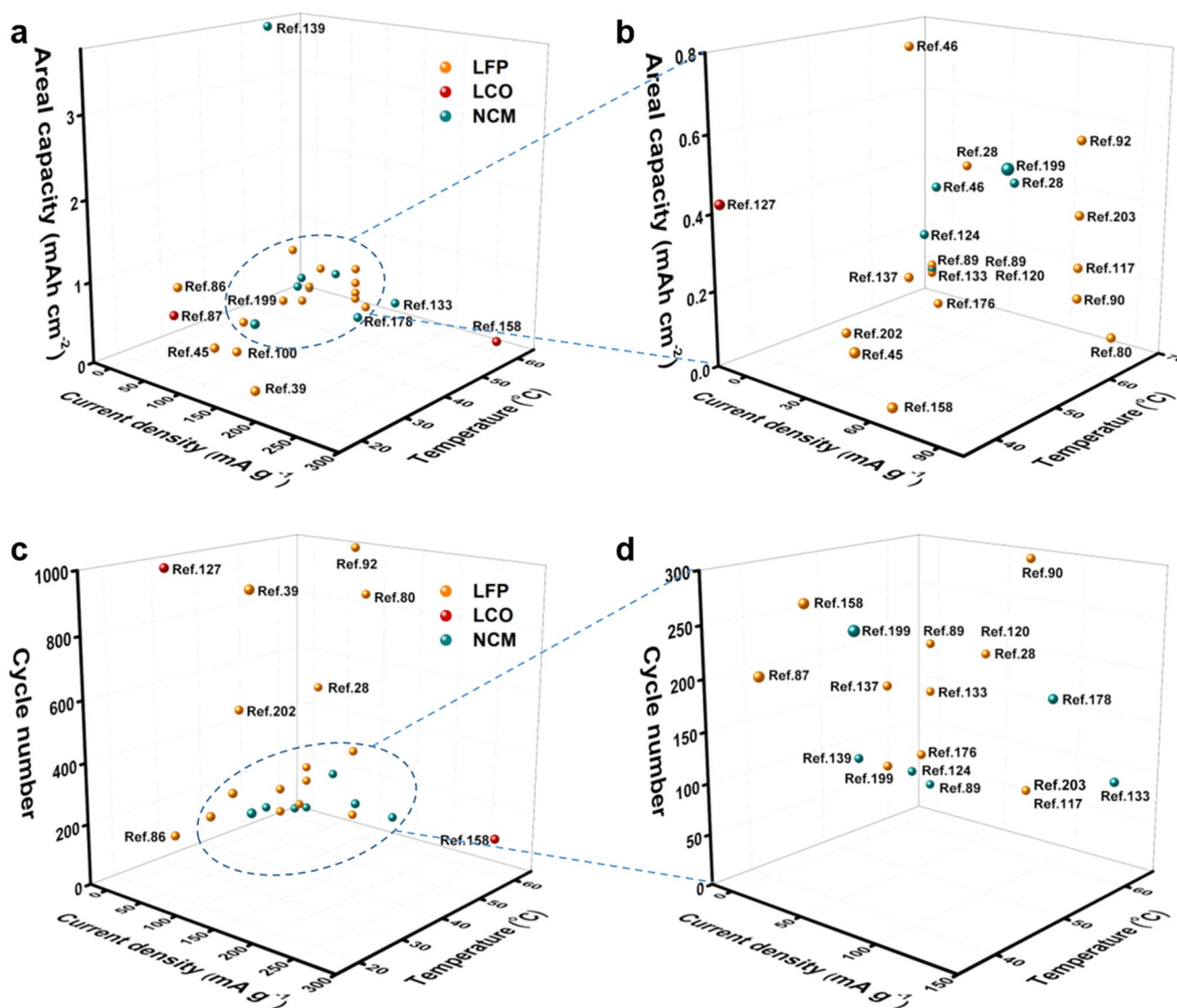


Fig. 12 The comparison of **a, b** areal capacity and **c, d** long cycles of lithium metal batteries at different current densities and temperatures

To further reduce the N/P ratio, a plating 4.1 mAh cm^{-2} of Li on the Cu was assembled with superior active material load ($17\text{--}20 \text{ mg cm}^{-2}$) cathode and ultrathin PAN/UFF/PEO CSE ($4.2 \mu\text{m}$), achieving a low N/P ratio of 1.1 and a good energy density of 506 Wh kg^{-1} and 1514 Wh L^{-1} [141]. Consequently, the cycling performance of a flexible pouch cell with PEO/ceramic CSEs was tested after cutting, folding, twisting, punching and burning (Fig. 13a–d) [83, 96, 197]. For example, at different degrees of bending, the pouch cell showed continuous and stable 30 cycles (Fig. 13b) and continues to light up the LED lamp after cutting, illustrating the safety and flexibility of the pouch cell [135]. However, the pouch cells with PEO/ceramic CSEs exhibit only dozens of times continuous charge and discharge. Therefore, a superior energy density of solid-state battery is closely related to CSEs, cathode and lithium anode, and crucially, is appropriate to a pouch cell for practical application.

5.2 SSLMB with Sulfur Cathode

Lithium-sulfur batteries are a kind of lithium metal batteries with elemental sulfur as cathode and lithium metal as anode. The working principle of lithium-sulfur batteries is as follows: lithium metal is oxidized to form Li^+ and electrons in the discharge process. The Li^+ moves to the sulfur cathode through electrolyte, and the electrons reach cathode through external circuit wire. Sulfur reacts with Li^+ and electrons to form Li_2S at the cathode with the formation of several soluble lithium polysulfide intermediates. The charging process is opposite. Lithium-sulfur batteries have a high theoretical specific capacity of 1671 mAh g^{-1} based on sulfur cathode, which is also naturally abundant, low cost, and environmentally friendly [198]. However, in addition to the problems mentioned similar with typical lithium metal batteries, they also face many notorious problems: low utilization of sulfur active material, the polysulfide shuttle effect, side reaction,

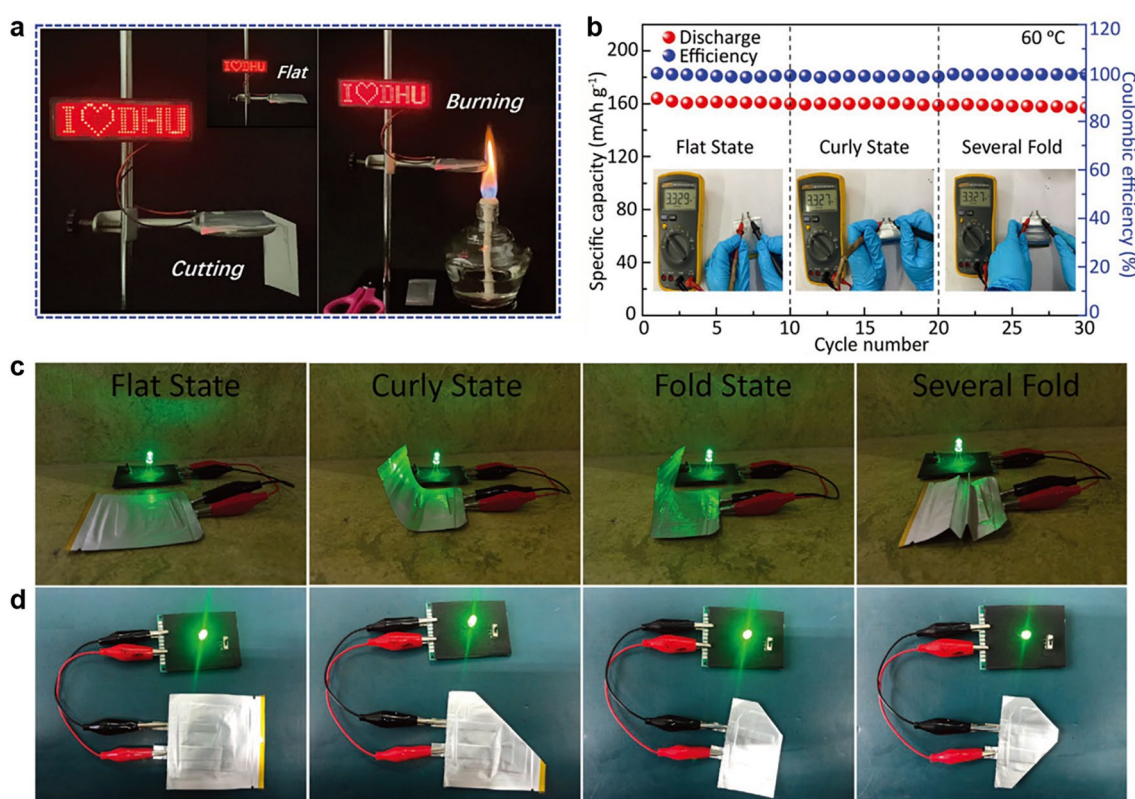


Fig. 13 **a** Test of LCO/Li pouch cell by lighting a LED under cutting and burning. Reproduced with permission [196]. Copyright 2020, Wiley–VCH. **b** Cyclic performance of LFP/Li pouch cell under different states at 0.1C, the insets are the voltage variation images of the pouch cell before and after curling and folding. **c** Optical photographs of the flexible LFP/Li pouch cell under different states, lighting up an LED in series. **d** Safety evaluation of LFP/Li pouch cell under extreme conditions. **b–d** Reproduced with permission [135]. Copyright 2021, Wiley–VCH

safety, poor electronic/ionic conductivity of sulfur and lithium sulfide (Li_2S), etc.

In recent years, PEO/ceramic CSEs have been widely applied in solid-state lithium-sulfur batteries (SSLSB) due to their high safety and capability to tackle the issue of sulfur cathode and Li anode [169, 199, 200]. For example, the incorporation of TiO_2 nanoparticles into PEO can suppress the undesired shuttle effect owing to dissolved lithium polysulfides (Fig. 14a–c) [201]. The cells with TiO_2 /PEO CSEs exhibited an improved capacity retention of $\sim 87\%$ after 100 cycles, higher than that of PEO electrolytes without TiO_2 nanoparticles ($\sim 38\%$). This is because polysulfide species are effectively withheld or trapped by the embedded TiO_2 nanoparticles to retard the polysulfide shuttling. Benefiting from the high specific capacity of sulfur, the SSLSB with MB-LLZTO CSEs exhibited a specific capacity of $\sim 1280 \text{ mAh g}^{-1}$ and capacity retention of 60% after 220 cycles (Fig. 14d). However, the battery with LiFePO_4 cathode exhibited a discharge capacity of only 140 mAh g^{-1} after 170 cycles (Fig. 14e) [98].

Similarly, the composite cathode with the electrolyte can enhance interface compatibility by increasing the contact area [130]. For example, Cui et al. [202] prepared a composite cathode (S@LLZO@C) by a thermal diffusion method and the dispersed LLZO nanoparticles acting as the interfacial stabilizer, which delivered a specific capacity of 1210 mAh g^{-1} , higher than that of the S@C cathode of 768 mAh g^{-1} (Fig. 15a, b). Moreover, larger potential hysteresis is observed in the voltage curves of the S@C cathode (Fig. 15c), indicating that the S@LLZO@C nanostructure can reduce the interface resistance to ensure high electronic and ionic conductivity simultaneously. In addition, the cells with thinner electrolytes that have a higher ionic conductance result in better cycle performance. For example, CSEs of 80 and 20 mg correspond to thicknesses of 520 ± 10 and $120 \pm 5 \mu\text{m}$, respectively. The cell with 20 mg CSE possessed a lower initial discharge capacity of 778.1 mAh g^{-1} , but a higher capacity retention of 93.2% after 100th cycle, as compared with the cell with 80 mg CSE (818.6 mAh g^{-1} , 77.9% (Fig. 15d). Meanwhile, the cell with 20 mg CSE exhibited lower interfacial impedances (Fig. 15e) and superior cycle performance (Fig. 15f) [203].

In addition, some challenges similar to typical lithium metal batteries, such as the high excess of lithium metal anode, the low areal capacity in sulfur cathode,

high N/P ratio, high operating temperature, should be cautiously considered for realizing high-energy-density SSLSB. At present, the majority of SSLSB with PEO/ceramic CSEs did not provide N/P ratio probably due to the use of excess of lithium anode (commercial lithium disc around of $400\text{--}500 \mu\text{m}$). Fortunately, a pressed Li foil with a thickness of $80 \mu\text{m}$ were coupled with sulfur cathode with 10.0 mg cm^{-2} of sulfur delivering a low N/P ratio of 1/1, and the cell exhibited a high areal capacity of 11.8 mAh cm^{-2} at 1 mA cm^{-2} [35], which is one of the record values among PEO/ceramic CSEs in SSLSB, to the best of our knowledge. Besides, vast majority of sulfur cathode showed a low sulfur loading ($0.5\text{--}3 \text{ mg cm}^{-2}$), and the cell delivered unsatisfactory the areal capacity ($< 2.0 \text{ mAh cm}^{-2}$), and the cells operated at a higher temperature ($> 36 \text{ }^\circ\text{C}$). More importantly, the pouch cells with PEO/ceramic CSEs are lacking. To our knowledge, only two cases were reported that can power LED lamps and operate for 90 cycles at 1 mA cm^{-2} [35, 98]. Therefore, optimizing CSEs, cathode and lithium anode is required for achieving an excellent energy density of SSLSB, especially for pouch cells of practical application.

6 Summary and Outlook

LMBs are considered to be a strong competitor over traditional lithium-ion batteries. However, the unsafety of using volatile and flammable organic liquid electrolytes prevents their practical applications. PEO/ceramic CSEs are promising substitutes for liquid electrolytes and have attracted wide attention in the research of energy storage systems. In this review, the critical issues of PEO/ceramic CSEs are specifically introduced. We emphasize fabricating strategies of PEO/ceramic CSEs, controlling interfacial compatibility and improving solid-state battery performance. Benefiting from the versatile preparation methods, PEO/ceramic CSEs can tackle the trade-off of ionic conductivity and mechanical properties. In addition, much effort has been made to increase interfacial compatibility, such as surface modification of ceramic particles, constructing chemical bonds and interface optimization of electrodes/CSEs. Regarding the application of full cells, we summarize solid-state lithium metal batteries with transition metal oxides and sulfur cathodes. To achieve high energy

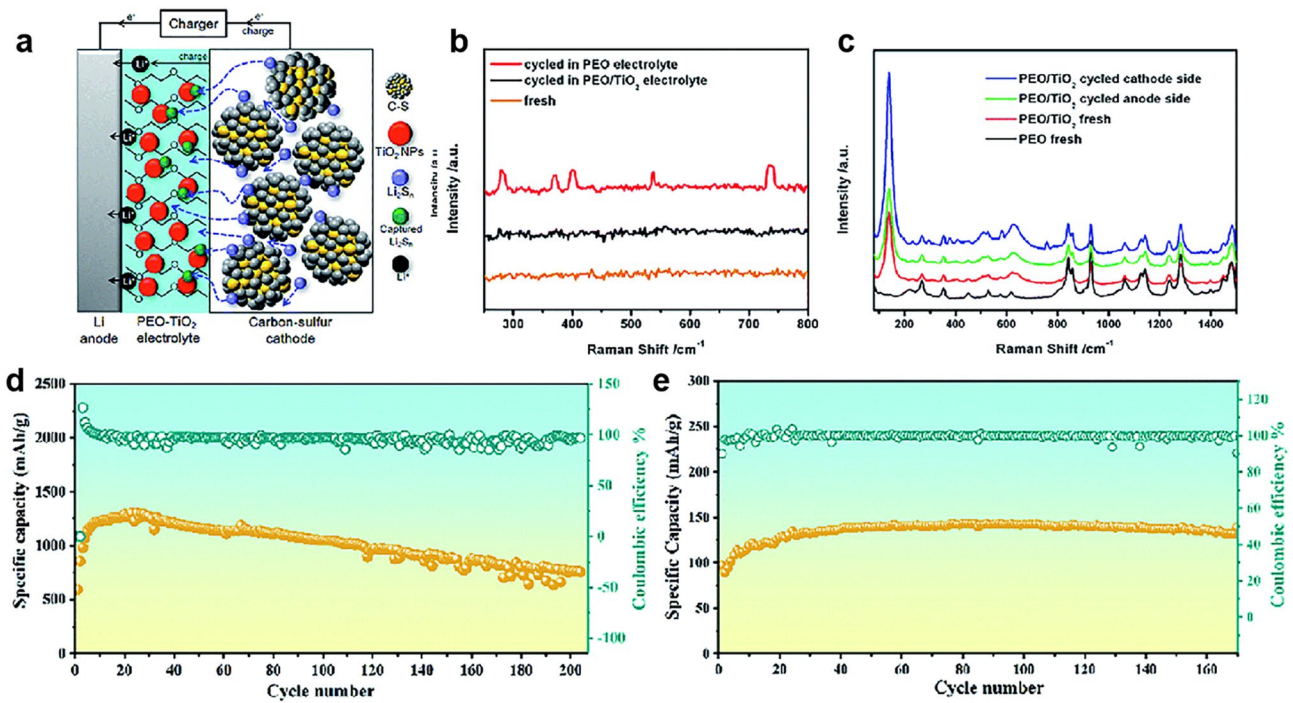


Fig. 14 **a** Schematic illustration of the inhibition of soluble Li_2S_n diffusion. Upon charging, Raman spectra of **b** Li anode and PEO and **c** PEO/ TiO_2 electrolytes before and after cycling. **a–c** Reproduced with permission [201]. Copyright 2017, Royal Society of Chemistry. **d** Discharge capacity and Coulombic efficiency of the Li–S battery based on MB–LLZTO CSE at 45 °C. **e** Discharge capacity and Coulombic efficiency of the MB–LLZTO CSE-based LFP–Li battery at 45 °C. **d, e** Reproduced with permission [98]. Copyright 2019, Royal Society of Chemistry

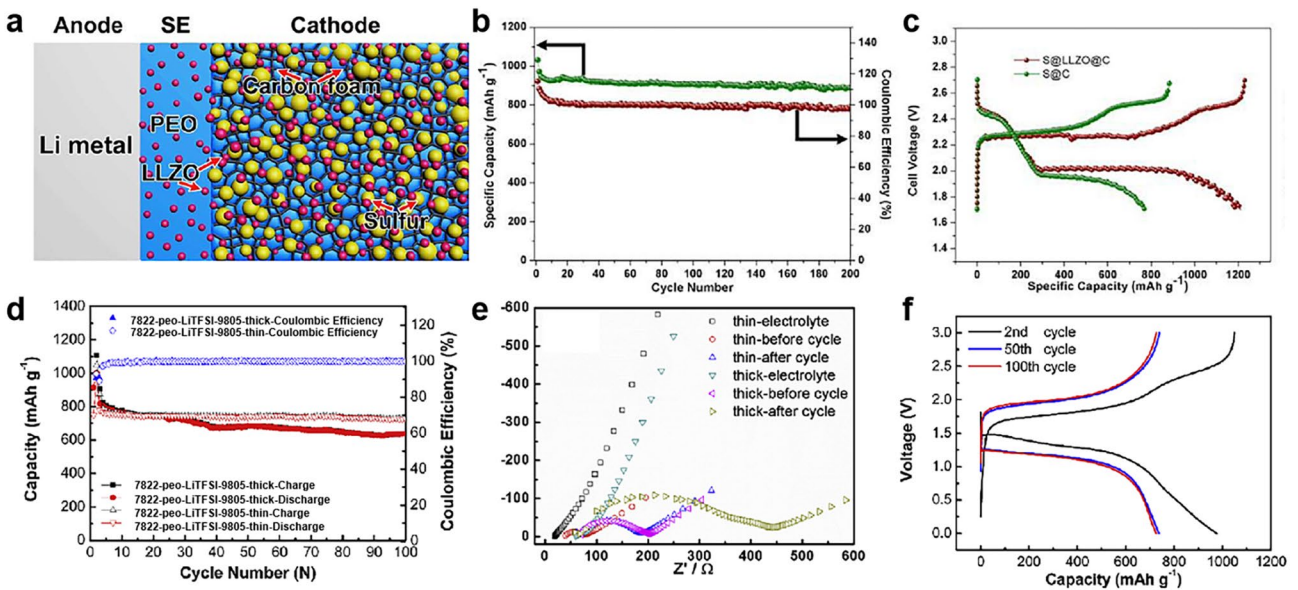


Fig. 15 **a** Schematic illustration of an SSLSB based on LLZO nanostructures. **b** Cycling performance and Coulombic efficiency of the S@LLZO@C cathode with a current density of 0.05 mA cm^{-2} at 37 °C. **c** Typical charge/discharge curves of the S@LLZO@C and S@C cathodes with 0.1 mA cm^{-2} at 50 °C. **a–c** Reproduced with permission [202]. Copyright 2017, American Chemical Society. **d** Cycle performance of S-CNT//7822-peo-LiTFSI-9505/Li-In all-solid-state cells. **e** Nyquist plots for the cells using 80 or 20 mg composite electrolytes before and after the 100th cycle. **f** The charge–discharge voltage profiles at the 2nd, 50th, and 100th cycles of the cells using 20 mg 7822-peo-LiTFSI-9505 as the electrolyte layers. **d–f** Reproduced with permission [203]. Copyright 2020, Elsevier

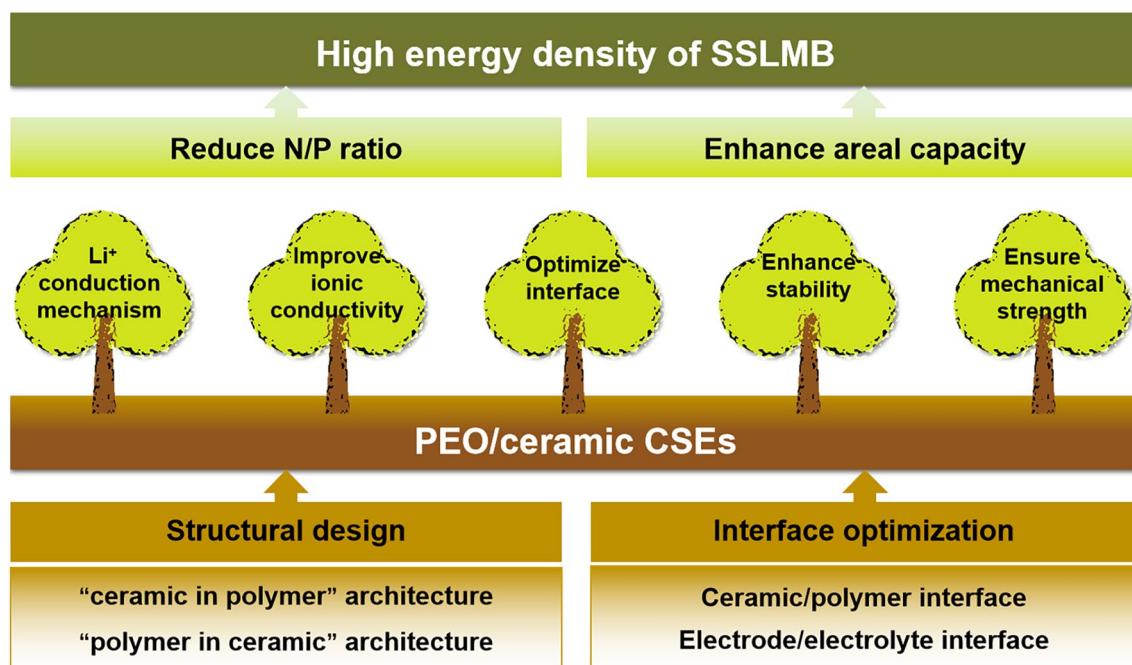


Fig. 16 Schematic illustration of significant challenges and strategies to achieve excellent SSLMB

density and safety of SSLMB, the research directions are proposed in the future (Fig. 16).

For PEO/ceramic CSEs: (a) Insightfully investigate Li^+ conduction mechanism or behavior. Theoretical calculations and advanced characterization techniques especially in situ tests are key to studying the local structural environments and dynamics of lithium ions to confirm the experimental results; (b) Improve ionic conductivity and reduce electronic conductivity at low operating temperatures. The vast majority of CSEs have an ionic conductivity of $\sim 10^{-4} \text{ S cm}^{-1}$ at room temperature, which still exhibits a gap compared with liquid electrolytes ($\sim 10^{-2} \text{ S cm}^{-1}$). At the same time, Li^+ transference number is enhanced to further clarify the ion mobility behavior; (c) Optimize interfacial contact. The described interface of CSEs mainly includes the interface of polymer/ceramic and CSEs/electrodes. The solid–solid interface seriously affects Li^+ transport, increasing internal resistance, thus deteriorating the cycle and rate performance of battery; (d) Reduce the thickness of CSEs and shorten ion conduction distance, while ensuring mechanical strength and flexibility. Reduced mass and volume can improve energy density of solid-state batteries.

From the viewpoint of SSLMB: (a) Reduce the thickness of lithium metal anode such as down to $20 \mu\text{m}$ (5 mAh cm^{-2}), which can greatly reduce N/P ratio and improve Li utilization to achieve high energy density; (b) Increase mass loading of active materials in cathode to achieve areal capacity close to or even beyond to current commercial Li-ion batteries (4 mAh cm^{-2}). Reducing the N/P ratio and enhancing areal capacity are significant for achieving an energy density of SSLMB; (c) Assemble pouch cells is necessary to evaluate their potential for commercialization. A superior energy density of solid-state batteries is closely related to CSEs, cathode and lithium anode. Not only that, suitable pressures are necessary to the pouch cells when designing the structure of pouch cells.

Upcoming efforts can focus on the design of multifunctional CSEs to match ultrathin lithium metal anodes and high-load cathodes for achieving a high energy density of SSLMB (500 Wh kg^{-1}). In addition, there is a strong demand for realizing large-scale production and increasing energy density and cycle stability. However, when the battery is magnified to a pouch cell, the problems mentioned above will be further magnified, which means that the cycle life of lithium metal anode with high capacity will be further shortened. Thus, precise control of the structure–performance relationship of CSEs

together with lithium metal anodes and cathodes beyond the laboratory level is necessary.

Acknowledgements This work was financially supported by National Key R&D Program for International Cooperation (No. 2021YFE0115100), the project of the National Natural Science Foundation of China (Nos. 51872240, 51972270 and 52172101), Key Research and Development Program of Shaanxi Province (No. 2021ZDLGY14-08 and 2022KWZ-04), Natural Science Foundation of Shaanxi Province (2020JZ-07), the Research Fund of the State Key Laboratory of Solidification Processing (NPU), China (2021-TS-03), the Fundamental Research Funds for the Central Universities (No. 3102019JC005 and G2022KY0604), and the Research Fund of the State Key Laboratory of Solid Lubrication (CAS), China (LSL-2007).

Funding Open access funding provided by Shanghai Jiao Tong University.

Open Access This article is licensed under a Creative Commons Attribution 4.0 International License, which permits use, sharing, adaptation, distribution and reproduction in any medium or format, as long as you give appropriate credit to the original author(s) and the source, provide a link to the Creative Commons licence, and indicate if changes were made. The images or other third party material in this article are included in the article's Creative Commons licence, unless indicated otherwise in a credit line to the material. If material is not included in the article's Creative Commons licence and your intended use is not permitted by statutory regulation or exceeds the permitted use, you will need to obtain permission directly from the copyright holder. To view a copy of this licence, visit <http://creativecommons.org/licenses/by/4.0/>.

References

- R.A. Barreto, Fossil fuels, alternative energy and economic growth. *Econ. Model.* **75**, 196–220 (2018). <https://doi.org/10.1016/j.econmod.2018.06.019>
- X.Q. Zhang, X.B. Cheng, Q. Zhang, Nanostructured energy materials for electrochemical energy conversion and storage: a review. *J. Energy Chem.* **25**, 967–984 (2016). <https://doi.org/10.1016/j.jechem.2016.11.003>
- Q. Zhang, L. Suresh, Q.J. Liang, Y.X. Zhang, L. Yang et al., Emerging technologies for green energy conversion and storage. *Adv. Sustain. Syst.* **5**, 2000152 (2021). <https://doi.org/10.1002/adsu.202000152>
- Y.L. Gao, Z.H. Pan, J.G. Sun, Z.L. Liu, J. Wang, High-energy batteries: beyond lithium-ion and their long road to commercialisation. *Nano-Micro Lett.* **14**, 94 (2022). <https://doi.org/10.1007/s40820-022-00844-2>
- T.Z. Xu, D. Wang, Z.W. Li, Z.Y. Chen, J.H. Zhang et al., Electrochemical proton storage: from fundamental understanding to materials to devices. *Nano-Micro Lett.* **14**, 126 (2022). <https://doi.org/10.1007/s40820-022-00864-y>
- G.E. Blomgren, The development and future of lithium ion batteries. *J. Electrochem. Soc.* **164**, A5019–A5025 (2017). <https://doi.org/10.1149/2.0251701jes>
- M. Li, J. Lu, Z.W. Chen, K. Amine, 30 years of lithium-ion batteries. *Adv. Mater.* **30**, 1800561 (2018). <https://doi.org/10.1002/adma.201800561>
- C.P. Grey, D.S. Hall, Prospects for lithium-ion batteries and beyond—a 2030 vision. *Nat. Commun.* **11**, 6279 (2020). <https://doi.org/10.1038/s41467-020-19991-4>
- T. Placke, R. Kloepsch, S. Dühnen, M. Winter, Lithium ion, lithium metal, and alternative rechargeable battery technologies: the odyssey for high energy density. *J. Solid State Electr.* **21**, 1939–1964 (2017). <https://doi.org/10.1007/s10008-017-3610-7>
- Q.Y. Wang, B. Liu, Y.H. Shen, J.K. Wu, Z.Q. Zhao et al., Confronting the challenges in lithium anodes for lithium metal batteries. *Adv. Sci.* **8**, 2101111 (2021). <https://doi.org/10.1002/advs.202101111>
- W. Xu, J.L. Wang, F. Ding, X.L. Chen, E. Nasybulin et al., Lithium metal anodes for rechargeable batteries. *Energy Environ. Sci.* **7**, 513–537 (2014). <https://doi.org/10.1039/c3ee40795k>
- X.Q. Min, G.J. Xu, B. Xie, P. Guan, M.L. Sun et al., Challenges of prelithiation strategies for next generation high energy lithium-ion batteries. *Energy Storage Mater.* **47**, 297–318 (2022). <https://doi.org/10.1016/j.ensm.2022.02.005>
- J.M. Wang, B.C. Ge, H. Li, M. Yang, J. Wang et al., Challenges and progresses of lithium-metal batteries. *Chem. Eng. J.* **420**, 129739 (2021). <https://doi.org/10.1016/j.ccej.2021.129739>
- H.S. Wang, Z.A. Yu, X. Kong, S.C. Kim, D.T. Boyle et al., Liquid electrolyte: The nexus of practical lithium metal batteries. *Joule* **6**, 588–616 (2022). <https://doi.org/10.1016/j.joule.2021.12.018>
- S.J. Tan, W.P. Wang, Y.F. Tian, S. Xin, Y.G. Guo, Advanced electrolytes enabling safe and stable rechargeable Li-metal batteries: progress and prospects. *Adv. Funct. Mater.* **31**, 2105253 (2021). <https://doi.org/10.1002/adfm.202105253>
- T.C. Liu, J.L. Wang, Y. Xu, Y.F. Zhang, Y. Wang, Dendrite-free and stable lithium metal battery achieved by a model of stepwise lithium deposition and stripping. *Nano-Micro Lett.* **13**, 170 (2021). <https://doi.org/10.1007/s40820-021-00687-3>
- Z.A. Yu, Y. Cui, Z.N. Bao, Design principles of artificial solid electrolyte interphases for lithium-metal anodes. *Cell Rep. Phys. Sci.* **1**, 100119 (2020). <https://doi.org/10.1016/j.xcrp.2020.100119>
- X.L. Fan, C.S. Wang, High-voltage liquid electrolytes for Li batteries: progress and perspectives. *Chem. Soc. Rev.* **50**, 10486–10566 (2021). <https://doi.org/10.1039/d1cs00450f>
- H. Lee, P. Oh, J. Kim, H. Cha, S. Chae et al., Advances and prospects of sulfide all-solid-state lithium batteries via one-to-one comparison with conventional liquid lithium ion batteries. *Adv. Mater.* **31**, 1900376 (2019). <https://doi.org/10.1002/adma.201900376>



20. Y. Zhang, T.T. Zuo, J. Popovic, K. Lim, Y.X. Yin et al., Towards better Li metal anodes: challenges and strategies. *Mater. Today* **30**, 56–74 (2019). <https://doi.org/10.1016/j.mattod.2019.09.018>
21. W.B. Wu, Y.Y. Bo, D.P. Li, Y.H. Liang, J.C. Zhang et al., Safe and stable lithium metal batteries enabled by an amide-based electrolyte. *Nano-Micro Lett.* **14**, 44 (2022). <https://doi.org/10.1007/s40820-021-00780-7>
22. W.H. Ren, C.F. Ding, X.W. Fu, Y. Huang, Advanced gel polymer electrolytes for safe and durable lithium metal batteries: challenges, strategies, and perspectives. *Energy Storage Mater.* **34**, 515–535 (2021). <https://doi.org/10.1016/j.ensm.2020.10.018>
23. X.Y. Li, Y. Wang, K. Xi, W. Yu, J. Feng et al., Quasi-solid-state ion-conducting arrays composite electrolytes with fast ion transport vertical-aligned interfaces for all-weather practical lithium-metal batteries. *Nano-Micro Lett.* **14**, 210 (2022). <https://doi.org/10.1007/s40820-022-00952-z>
24. J.G. Yi, L. Chen, Y.C. Liu, H.X. Geng, L.Z. Fan, High capacity and superior cyclic performances of all-solid-state lithium-sulfur batteries enabled by a high-conductivity $\text{Li}_{10}\text{SnP}_2\text{S}_{12}$ solid electrolyte. *ACS Appl. Mater. Interfaces* **11**, 36774–36781 (2019). <https://doi.org/10.1021/acsami.9b12846>
25. Y. Lu, X.Y. Meng, J.A. Alonso, M.T. Fernández-Díaz, C.W. Sun, Effects of fluorine doping on structural and electrochemical properties of $\text{Li}_{6.25}\text{Ga}_{0.25}\text{La}_3\text{Zr}_2\text{O}_{12}$ as electrolytes for solid-state lithium batteries. *ACS Appl. Mater. Interfaces* **11**, 2042–2049 (2019). <https://doi.org/10.1021/acsami.8b17656>
26. Z.Y. Lin, X.W. Guo, Y.B. Yang, M.X. Tang, Q. Wei et al., Block copolymer electrolyte with adjustable functional units for solid polymer lithium metal battery. *J. Energy Chem.* **52**, 67–74 (2021). <https://doi.org/10.1016/j.jechem.2020.04.052>
27. Z.C. Tian, D. Kim, A flexible, robust, and high ion-conducting solid electrolyte membranes enabled by interpenetrated network structure for all-solid-state lithium metal battery. *J. Energy Chem.* **68**, 603–611 (2022). <https://doi.org/10.1016/j.jechem.2021.12.035>
28. S. Wang, Q.F. Sun, W.X. Peng, Y. Ma, Y. Zhou et al., Ameliorating the interfacial issues of all-solid-state lithium metal batteries by constructing polymer/inorganic composite electrolyte. *J. Energy Chem.* **58**, 85–93 (2021). <https://doi.org/10.1016/j.jechem.2020.09.033>
29. S. Li, S.Q. Zhang, L. Shen, Q. Liu, J.B. Ma et al., Progress and perspective of ceramic/polymer composite solid electrolytes for lithium batteries. *Adv. Sci.* **7**, 1903088 (2020). <https://doi.org/10.1002/adv.201903088>
30. C.T. Zhao, Q. Sun, J. Luo, J.N. Liang, Y.L. Liu et al., 3D porous garnet/gel polymer hybrid electrolyte for safe solid-state Li-O_2 batteries with long lifetimes. *Chem. Mater.* **32**, 10113–10119 (2020). <https://doi.org/10.1021/acs.chemmater.0c03529>
31. X.Y. Liu, X.R. Li, H.X. Li, H.B. Wu, Recent progress of hybrid solid-state electrolytes for lithium batteries. *Chem. Eur. J.* **24**, 18293–18306 (2018). <https://doi.org/10.1002/chem.201803616>
32. J. Wan, J. Xie, D.G. Mackanic, W. Burke, Z. Bao et al., Status, promises, and challenges of nanocomposite solid-state electrolytes for safe and high performance lithium batteries. *Mater. Today Nano* **4**, 1–16 (2018). <https://doi.org/10.1016/j.mtnano.2018.12.003>
33. Q.Q. Zhang, K. Liu, F. Ding, X.J. Liu, Recent advances in solid polymer electrolytes for lithium batteries. *Nano Res.* **10**, 4139–4174 (2017). <https://doi.org/10.1007/s12274-017-1763-4>
34. S.V. Ganesan, K.K. Mothilal, S. Selvasekarapandian, T.K. Ganesan, The effect of titanium dioxide nano-filler on the conductivity, morphology and thermal stability of poly(methyl methacrylate)-poly(styrene-co-acrylonitrile) based composite solid polymer electrolytes. *J. Mater. Sci. Mater. Electron.* **29**, 8089–8099 (2018). <https://doi.org/10.1007/s10854-018-8815-8>
35. F. Pei, S.Q. Dai, B.F. Guo, H. Xie, C.W. Zhao et al., Titanium-oxo cluster reinforced gel polymer electrolyte enabling lithium-sulfur batteries with high gravimetric energy densities. *Energy Environ. Sci.* **14**, 975–985 (2021). <https://doi.org/10.1039/d0ee03005h>
36. D.C. Zhang, Z.B. Liu, Y.W. Wu, S.M. Ji, Z.X. Yuan et al., In situ construction a stable protective layer in polymer electrolyte for ultralong lifespan solid-state lithium metal batteries. *Adv. Sci.* **9**, 2104277 (2022). <https://doi.org/10.1002/adv.202104277>
37. W. Fan, X.L. Zhang, C.J. Li, S.Y. Zha, J. Wang, UV-initiated soft-tough multifunctional gel polymer electrolyte achieves stable-cycling Li-metal battery. *ACS Appl. Energy Mater.* **2**, 4513–4520 (2019). <https://doi.org/10.1021/acsaem.9b00766>
38. Y.Y. Yan, J.W. Ju, S.M. Dong, Y.T. Wang, L. Huang et al., In situ polymerization permeated three-dimensional Li-percolated porous oxide ceramic framework boosting all solid-state lithium metal battery. *Adv. Sci.* **8**, 2003887 (2021). <https://doi.org/10.1002/adv.202003887>
39. S. Li, J.Z. Lu, Z. Geng, Y. Chen, X.Q. Yu et al., Solid polymer electrolyte reinforced with a $\text{Li}_{1.3}\text{Al}_{0.3}\text{Ti}_{1.7}(\text{PO}_4)_3$ -coated separator for all-solid-state lithium batteries. *ACS Appl. Mater. Interfaces* **14**, 1195–1202 (2022). <https://doi.org/10.1021/acsami.1c21804>
40. B. Chen, Z. Huang, X.T. Chen, Y.R. Zhao, Q. Xu et al., A new composite solid electrolyte $\text{PEO/Li}_{10}\text{GeP}_2\text{S}_{12}/\text{SN}$ for all-solid-state lithium battery. *Electrochim. Acta* **210**, 905–914 (2016). <https://doi.org/10.1016/j.electacta.2016.06.025>
41. M. Keller, G.B. Appetecchi, G.T. Kim, V. Sharova, M. Schneider et al., Electrochemical performance of a solvent-free hybrid ceramic-polymer electrolyte based on $\text{Li}_7\text{La}_3\text{Zr}_2\text{O}_{12}$ in $\text{P}(\text{EO})_{15}\text{LiTFSI}$. *J. Power Sources* **353**, 287–297 (2017). <https://doi.org/10.1016/j.jpowsour.2017.04.014>
42. W.P. Chen, H. Duan, J.L. Shi, Y.M. Qian, J. Wan et al., Bridging interparticle Li^+ conduction in a soft ceramic oxide electrolyte. *J. Am. Chem. Soc.* **143**, 5717–5726 (2021). <https://doi.org/10.1021/jacs.0c12965>

43. B. Huang, B.Y. Xu, J.X. Zhang, Z.H. Li, Z.Y. Huang et al., Li-ion conductivity and stability of hot-pressed LiTa_2PO_8 solid electrolyte for all-solid-state batteries. *J. Mater. Sci.* **56**, 2425–2434 (2020). <https://doi.org/10.1007/s10853-020-05324-9>
44. A.J. Blake, R.R. Kohlmeyer, J.O. Hardin, E.A. Carmona, B. Maruyama et al., 3D printable ceramic-polymer electrolytes for flexible high-performance Li-ion batteries with enhanced thermal stability. *Adv. Energy Mater.* **7**, 1602920 (2017). <https://doi.org/10.1002/aenm.201602920>
45. P.C. Yao, B. Zhu, H.W. Zhai, X.B. Liao, Y.X. Zhu et al., PVDF/palygorskite nanowire composite electrolyte for 4 V rechargeable lithium batteries with high energy density. *Nano Lett.* **18**, 6113–6120 (2018). <https://doi.org/10.1021/acs.nanolett.8b01421>
46. B.Y. Xu, X.Y. Li, C. Yang, Y.T. Li, N.S. Grundish et al., Interfacial chemistry enables stable cycling of all-solid-state Li metal batteries at high current densities. *J. Am. Chem. Soc.* **143**, 6542–6550 (2021). <https://doi.org/10.1021/jacs.1c00752>
47. O.W. Sheng, H.L. Hu, T.F. Liu, Z.J. Ju, G.X. Lu et al., Interfacial and ionic modulation of poly(ethylene oxide) electrolyte via localized iodization to enable dendrite-free lithium metal batteries. *Adv. Funct. Mater.* **32**, 2111026 (2021). <https://doi.org/10.1002/adfm.202111026>
48. Y. Xia, X.L. Wang, X.H. Xia, R.C. Xu, S.Z. Zhang et al., A newly designed composite gel polymer electrolyte based on poly(vinylidene fluoride-hexafluoropropylene) (PVDF-HFP) for enhanced solid-state lithium-sulfur batteries. *Chemistry* **23**, 15203–15209 (2017). <https://doi.org/10.1002/chem.201703464>
49. X.R. Yu, L.L. Wang, J. Ma, X.W. Sun, X.H. Zhou et al., Selectively wetted rigid-flexible coupling polymer electrolyte enabling superior stability and compatibility of high-voltage lithium metal batteries. *Adv. Energy Mater.* **10**, 1903939 (2020). <https://doi.org/10.1002/aenm.201903939>
50. M.J. Lee, J.H. Han, K. Lee, Y.J. Lee, B.G. Kim et al., Elastomeric electrolytes for high-energy solid-state lithium batteries. *Nature* **601**, 217–222 (2022). <https://doi.org/10.1038/s41586-021-04209-4>
51. Y. Zhang, W. Feng, Y.C. Zhen, P.Y. Zhao, X.H. Wang et al., Effects of lithium salts on PEO-based solid polymer electrolytes and their all-solid-state lithium-ion batteries. *Ionics* **28**, 2751–2758 (2022). <https://doi.org/10.1007/s11581-022-04525-3>
52. R.A. Tong, L.H. Chen, B.B. Fan, G. Shao, R.P. Liu et al., Solvent-free process for blended PVDF-HFP/PEO and LLZTO composite solid electrolytes with enhanced mechanical and electrochemical properties for lithium metal batteries. *ACS Appl. Energy Mater.* **4**, 11802–11812 (2021). <https://doi.org/10.1021/acsaem.1c02566>
53. Y.X. Ma, J.Y. Wan, Y.F. Yang, Y.S. Ye, X. Xiao et al., Scalable, ultrathin, and high-temperature-resistant solid polymer electrolytes for energy-dense lithium metal batteries. *Adv. Energy Mater.* **12**, 2103720 (2022). <https://doi.org/10.1002/aenm.202103720>
54. D.E. Fenton, J.M. Parker, P.V. Wright, Complexes of alkali metal ions with poly(ethylene oxide). *Polymer* **14**, 589 (1973). [https://doi.org/10.1016/0032-3861\(73\)90146-8](https://doi.org/10.1016/0032-3861(73)90146-8)
55. S. Lascaud, M. Perrier, A. Vallée, S. Besner, J. Prud'homme, Phase diagrams and conductivity behavior of poly(ethylene oxide)-molten salt rubbery electrolytes. *Macromolecules* **27**, 7469–7477 (1994). <https://doi.org/10.1021/ma00103a034>
56. E. Quartarone, P. Mustarelli, A. Magistris, PEO-based composite polymer electrolytes. *Solid State Ionics* **110**, 1–14 (1998). [https://doi.org/10.1016/S0167-2738\(98\)00114-3](https://doi.org/10.1016/S0167-2738(98)00114-3)
57. P. Fan, H. Liu, V. Marosz, N.T. Samuels, S.L. Suib et al., High performance composite polymer electrolytes for lithium-ion batteries. *Adv. Funct. Mater.* **31**, 2101380 (2021). <https://doi.org/10.1002/adfm.202101380>
58. J.L. Qiu, X.Y. Liu, R.S. Chen, Q.H. Li, Y. Wang et al., Enabling stable cycling of 4.2 V high-voltage all-solid-state batteries with PEO-based solid electrolyte. *Adv. Funct. Mater.* **30**, 1909392 (2020). <https://doi.org/10.1002/adfm.201909392>
59. K.H. Nie, X.L. Wang, J.L. Qiu, Y. Wang, Q. Yang et al., Increasing poly(ethylene oxide) stability to 4.5 V by surface coating of the cathode. *ACS Energy Lett.* **5**, 826–832 (2020). <https://doi.org/10.1021/acscenergylett.9b02739>
60. F. Croce, G.B. Appetecchi, L. Persi, B. Scrosati, Nanocomposite polymer electrolytes for lithium batteries. *Nature* **394**, 456–458 (1998). <https://doi.org/10.1038/28818>
61. J.Y. Wu, L.X. Yuan, W.X. Zhang, Z. Li, X.L. Xie et al., Reducing the thickness of solid-state electrolyte membranes for high-energy lithium batteries. *Energy Environ. Sci.* **4**, 12–36 (2021). <https://doi.org/10.1039/d0ee02241a>
62. J. Popovic, D. Brandell, S. Ohno, K.B. Hatzel, J. Zheng et al., Polymer-based hybrid battery electrolytes: theoretical insights, recent advances and challenges. *J. Mater. Chem. A* **9**, 6050–6069 (2021). <https://doi.org/10.1039/d0ta11679c>
63. X.E. Wang, R. Kerr, F.F. Chen, N. Goujon, J.M. Pringle et al., Toward high-energy-density lithium metal batteries: opportunities and challenges for solid organic electrolytes. *Adv. Mater.* **32**, 1905219 (2020). <https://doi.org/10.1002/adma.201905219>
64. L.L. Du, B. Zhang, X.F. Wang, C.H. Dong, L.Q. Mai et al., 3D frameworks in composite polymer electrolytes: synthesis, mechanisms, and applications. *Chem. Eng. J.* **451**, 138787 (2023). <https://doi.org/10.1016/j.cej.2022.138787>
65. N. Meng, X.G. Zhu, F. Lian, Particles in composite polymer electrolyte for solid-state lithium batteries: a review. *Particulology* **60**, 14–36 (2022). <https://doi.org/10.1016/j.partic.2021.04.002>
66. Z.C. Shen, Y.F. Cheng, S.H. Sun, X. Ke, L.Y. Liu et al., The critical role of inorganic nanofillers in solid polymer composite electrolyte for Li^+ transportation. *Carbon Energy* **3**, 482–508 (2021). <https://doi.org/10.1002/cey2.108>
67. J. Feng, L. Wang, Y. Chen, P. Wang, H. Zhang et al., PEO based polymer-ceramic hybrid solid electrolytes: a review. *Nano Converg.* **8**, 2 (2021). <https://doi.org/10.1186/s40580-020-00252-5>



68. L.Z. Fan, H.C. He, C.W. Nan, Tailoring inorganic-polymer composites for the mass production of solid-state batteries. *Nat. Rev. Mater.* **6**, 1003–1019 (2021). <https://doi.org/10.1038/s41578-021-00320-0>
69. Y. Zheng, Y.Z. Yao, J.H. Ou, M. Li, D. Luo et al., A review of composite solid-state electrolytes for lithium batteries: fundamentals, key materials and advanced structures. *Chem. Soc. Rev.* **49**, 8790–8839 (2020). <https://doi.org/10.1039/d0cs00305k>
70. S. Tang, W. Guo, Y.Z. Fu, Advances in composite polymer electrolytes for lithium batteries and beyond. *Adv. Energy Mater.* **11**, 2000802 (2020). <https://doi.org/10.1002/aenm.202000802>
71. S. Kalnaus, A.S. Sabau, W.E. Tenhaeff, N.J. Dudney, C. Daniel, Design of composite polymer electrolytes for Li ion batteries based on mechanical stability criteria. *J. Power Sources* **201**, 280–287 (2012). <https://doi.org/10.1016/j.jpowsour.2011.11.020>
72. J. Zheng, P.B. Wang, H.Y. Liu, Y.Y. Hu, Interface-enabled ion conduction in $\text{Li}_{10}\text{GeP}_2\text{S}_{12}$ -poly(ethylene oxide) hybrid electrolytes. *ACS Appl. Energy Mater.* **2**, 1452–1459 (2019). <https://doi.org/10.1021/acsaeam.8b02008>
73. J. Zheng, H. Dang, X.Y. Feng, P.H. Chien, Y.Y. Hu, Li-ion transport in a representative ceramic-polymer-plasticizer composite electrolyte: $\text{Li}_7\text{La}_3\text{Zr}_2\text{O}_{12}$ -polyethylene oxide-tetraethylene glycol dimethyl ether. *J. Mater. Chem. A* **5**, 18457–18463 (2017). <https://doi.org/10.1039/c7ta05832b>
74. S.L. Liu, W.Y. Liu, D.L. Ba, Y.Z. Zhao, Y.H. Ye et al., Filler-integrated composite polymer electrolyte for solid-state lithium batteries. *Adv. Mater.* **35**, 2110423 (2023). <https://doi.org/10.1002/adma.202110423>
75. L. Chen, Y.T. Li, S.P. Li, L.Z. Fan, C.W. Nan et al., PEO/garnet composite electrolytes for solid-state lithium batteries: from “ceramic-in-polymer” to “polymer-in-ceramic.” *Nano Energy* **46**, 176–184 (2018). <https://doi.org/10.1016/j.nanoen.2017.12.037>
76. C. Wang, T.Q. Yang, W.K. Zhang, H. Huang, Y.P. Gan et al., Hydrogen bonding enhanced SiO_2 /PEO composite electrolytes for solid-state lithium batteries. *J. Mater. Chem. A* **10**, 3400–3408 (2022). <https://doi.org/10.1039/d1ta10607d>
77. J. Zheng, Y.Y. Hu, New insights into the compositional dependence of Li-ion transport in polymer-ceramic composite electrolytes. *ACS Appl. Mater. Interfaces* **10**, 4113–4120 (2018). <https://doi.org/10.1021/acsami.7b17301>
78. N. Wu, P.H. Chien, Y.T. Li, A. Dolocan, H.H. Xu et al., Fast Li^+ conduction mechanism and interfacial chemistry of a NASICON/polymer composite electrolyte. *J. Am. Chem. Soc.* **142**, 2497–2505 (2020). <https://doi.org/10.1021/jacs.9b12233>
79. H. Chen, M. Zheng, S. Qian, H.Y. Ling, Z. Wu et al., Functional additives for solid polymer electrolytes in flexible and high-energy-density solid-state lithium-ion batteries. *Carbon Energy* **3**, 929–956 (2021). <https://doi.org/10.1002/cey2.146>
80. Y.X. Su, F. Xu, Y.Q. Qiu, J.B. Zhang, X.R. Zhang et al., Electrolyte based on laser-generated nano-garnet in poly(ethylene oxide) for solid-state lithium metal batteries. *Chem. Eng. J.* **443**, 136418 (2022). <https://doi.org/10.1016/j.cej.2022.136418>
81. Q.W. Pan, Y.W. Zheng, S. Kota, W.C. Huang, S.J. Wang et al., 2D MXene-containing polymer electrolytes for all-solid-state lithium metal batteries. *Nanoscale Adv.* **1**, 395–402 (2019). <https://doi.org/10.1039/c8na00206a>
82. X.K. Zhang, J. Xie, F.F. Shi, D.C. Lin, Y.Y. Liu et al., Vertically aligned and continuous nanoscale ceramic-polymer interfaces in composite solid polymer electrolytes for enhanced ionic conductivity. *Nano Lett.* **18**, 3829–3838 (2018). <https://doi.org/10.1021/acs.nanolett.8b01111>
83. R. Fan, C. Liu, K.Q. He, S.H. Cheng, D.Z. Chen et al., Versatile strategy for realizing flexible room-temperature all-solid-state battery through a synergistic combination of salt affluent PEO and $\text{Li}_{6.75}\text{La}_3\text{Zr}_{1.75}\text{Ta}_{0.25}\text{O}_{12}$ nanofibers. *ACS Appl. Mater. Interfaces* **12**, 7222–7231 (2020). <https://doi.org/10.1021/acsami.9b20104>
84. W. Liu, S.W. Lee, D.C. Lin, F.F. Shi, S. Wang et al., Enhancing ionic conductivity in composite polymer electrolytes with well-aligned ceramic nanowires. *Nat. Energy* **2**, 17035 (2017). <https://doi.org/10.1038/nenergy.2017.35>
85. Z.J. Sun, Y.H. Li, S.Y. Zhang, L. Shi, H. Wu et al., $\text{g-C}_3\text{N}_4$ nanosheets enhanced solid polymer electrolytes with excellent electrochemical performance, mechanical properties, and thermal stability. *J. Mater. Chem. A* **7**, 11069–11076 (2019). <https://doi.org/10.1039/c9ta00634f>
86. H.W. An, Q.S. Liu, J.L. An, S.T. Liang, X.F. Wang et al., Coupling two-dimensional fillers with polymer chains in solid polymer electrolyte for room-temperature dendrite-free lithium-metal batteries. *Energy Storage Mater.* **43**, 358–364 (2021). <https://doi.org/10.1016/j.ensm.2021.09.019>
87. Y.Z. Shi, B. Li, Q. Zhu, K. Shen, W.J. Tang et al., MXene-based mesoporous nanosheets toward superior lithium ion conductors. *Adv. Energy Mater.* **10**, 1903534 (2020). <https://doi.org/10.1002/aenm.201903534>
88. W.J. Tang, S. Tang, C.J. Zhang, Q.T. Ma, Q. Xiang et al., Simultaneously enhancing the thermal stability, mechanical modulus, and electrochemical performance of solid polymer electrolytes by incorporating 2D sheets. *Adv. Energy Mater.* **8**, 1800866 (2018). <https://doi.org/10.1002/aenm.201800866>
89. J. Cheng, G.M. Hou, Q. Chen, D.P. Li, K.K. Li et al., Sheet-like garnet structure design for upgrading PEO-based electrolyte. *Chem. Eng. J.* **429**, 132343 (2022). <https://doi.org/10.1016/j.cej.2021.132343>
90. Y.H. Li, Z.J. Sun, D.Y. Liu, Y.Y. Gao, Y.K. Wang et al., A composite solid polymer electrolyte incorporating MnO_2 nanosheets with reinforced mechanical properties and electrochemical stability for lithium metal batteries. *J. Mater. Chem. A* **8**, 2021–2032 (2020). <https://doi.org/10.1039/c9ta11542k>
91. T. Li, B. Ding, J. Wang, Z.Y. Qin, J.F.S. Fernando et al., Sandwich-structured ordered mesoporous polydopamine/MXene hybrids as high-performance anodes for lithium-ion batteries. *ACS Appl. Mater. Interfaces* **12**, 14993–15001 (2020). <https://doi.org/10.1021/acsami.9b18883>

92. X.W. Yu, A. Manthiram, A long cycle life, all-solid-state lithium battery with a ceramic-polymer composite electrolyte. *ACS Appl. Energ. Mater.* **3**, 2916–2924 (2020). <https://doi.org/10.1021/acsaem.9b02547>
93. J. Cheng, G.M. Hou, Q. Sun, Z. Liang, X.Y. Xu et al., Cold-pressing PEO/LAGP composite electrolyte for integrated all-solid-state lithium metal battery. *Solid State Ion.* **345**, 115156 (2020). <https://doi.org/10.1016/j.ssi.2019.115156>
94. G.M. Hou, M.Q. Zhang, Y.F. Huang, W.H. Ruan, A TiO₂/PEO composite incorporated with in situ synthesized hyper-branched poly(amine-ester) and its application as a polymer electrolyte. *RSC Adv.* **6**, 83406–83411 (2016). <https://doi.org/10.1039/c6ra15351h>
95. J.A. Isaac, D. Devaux, R. Bouchet, Dense inorganic electrolyte particles as a lever to promote composite electrolyte conductivity. *Nat. Mater.* **21**, 1412–1418 (2022). <https://doi.org/10.1038/s41563-022-01343-w>
96. J.X. Zhang, N. Zhao, M. Zhang, Y.Q. Li, P.K. Chu et al., Flexible and ion-conducting membrane electrolytes for solid-state lithium batteries: Dispersion of garnet nanoparticles in insulating polyethylene oxide. *Nano Energy* **28**, 447–454 (2016). <https://doi.org/10.1016/j.nanoen.2016.09.002>
97. K.Q. He, S.H. Cheng, J.Y. Hu, Y.Q. Zhang, H.W. Yang et al., In-situ intermolecular interaction in composite polymer electrolyte for ultralong life quasi-solid-state lithium metal batteries. *Angew. Chem. Int. Ed.* **60**, 12116–12123 (2021). <https://doi.org/10.1002/anie.202103403>
98. W.W. Li, C.Z. Sun, J. Jin, Y.P. Li, C.H. Chen et al., Realization of the Li⁺ domain diffusion effect via constructing molecular brushes on the LLZTO surface and its application in all-solid-state lithium batteries. *J. Mater. Chem. A* **7**, 27304–27312 (2019). <https://doi.org/10.1039/c9ta10400c>
99. N. Wu, P.H. Chien, Y.M. Qian, Y.T. Li, H.H. Xu et al., Enhanced surface interactions enable fast Li⁺ conduction in oxide-polymer composite electrolyte. *Angew. Chem. Int. Ed.* **59**, 4131–4137 (2020). <https://doi.org/10.1002/anie.201914478>
100. D.C. Lin, P.Y. Yuen, Y.Y. Liu, W. Liu, N. Liu et al., A silica-aerogel-reinforced composite polymer electrolyte with high ionic conductivity and high modulus. *Adv. Mater.* **30**, 1802661 (2018). <https://doi.org/10.1002/adma.201802661>
101. Z. Li, W.X. Sha, X. Guo, Three-dimensional garnet framework-reinforced solid composite electrolytes with high lithium-ion conductivity and excellent stability. *ACS Appl. Mater. Interfaces* **11**, 26920–26927 (2019). <https://doi.org/10.1021/acsaami.9b07830>
102. J. ZagóRski, J.M.L.P.D. Amo, M.J. Cordill, Fdr Aguesse, L. Buannic et al., Garnet-polymer composite electrolytes: new insights on local Li-ion dynamics and electrodeposition stability with Li metal anodes. *ACS Appl. Energy Mater.* **2**, 1724–1746 (2019). <https://doi.org/10.1021/acsaem.8b01850>
103. M. Liu, S. Ganapathy, M. Wagemaker, A direct view on Li-ion transport and Li-metal plating in inorganic and hybrid solid-state electrolytes. *Acc. Chem. Res.* **55**, 333–344 (2022). <https://doi.org/10.1021/acs.accounts.1c00618>
104. J. Zheng, M.X. Tang, Y.Y. Hu, Lithium ion pathway within Li₇La₃Zr₂O₁₂-polyethylene oxide composite electrolytes. *Angew. Chem. Int. Ed.* **55**, 12538–12542 (2016). <https://doi.org/10.1002/anie.201607539>
105. M.R. Li, M. Kolek, J.E. Frerichs, W. Sun, X. Hou et al., Investigation of polymer/ceramic composite solid electrolyte system: the case of PEO/LGPs composite electrolytes. *ACS Sustain. Chem. Eng.* **9**, 11314–11322 (2021). <https://doi.org/10.1021/acssuschemeng.1c00904>
106. Y.Z. Zhu, X.F. He, Y.F. Mo, First principles study on electrochemical and chemical stability of solid electrolyte-electrode interfaces in all-solid-state Li-ion batteries. *J. Mater. Chem. A* **4**, 3253–3266 (2016). <https://doi.org/10.1039/c5ta08574h>
107. S.S. Chi, Y.C. Liu, N. Zhao, X.X. Guo, C.W. Nan et al., Solid polymer electrolyte soft interface layer with 3D lithium anode for all-solid-state lithium batteries. *Energy Storage Mater.* **17**, 309–316 (2019). <https://doi.org/10.1016/j.ensm.2018.07.004>
108. S.J. Pennycook, C.J. Li, M.S. Li, C.H. Tang, E. Okunishi et al., Material structure, properties, and dynamics through scanning transmission electron microscopy. *J. Anal. Sci. Technol.* **9**, 11 (2018). <https://doi.org/10.1186/s40543-018-0142-4>
109. Q. Cheng, A.J. Li, N. Li, S. Li, A. Zangiabadi et al., Stabilizing solid electrolyte-anode interface in Li-metal batteries by boron nitride-based nanocomposite coating. *Joule* **3**, 1510–1522 (2019). <https://doi.org/10.1016/j.joule.2019.03.022>
110. M. Liu, C. Wang, Z. Cheng, S. Ganapathy, L.A. Haverkate et al., Controlling the lithium-metal growth to enable low-lithium-metal-excess all-solid-state lithium-metal batteries. *ACS Mater. Lett.* **2**, 665–670 (2020). <https://doi.org/10.1021/acsmaterialslett.0c00152>
111. Y. Cheng, L.Q. Zhang, Q.B. Zhang, J. Li, Y.F. Tang et al., Understanding all solid-state lithium batteries through in situ transmission electron microscopy. *Mater. Today* **42**, 137–161 (2020). <https://doi.org/10.1016/j.mattod.2020.09.003>
112. C.C. Zhang, Y.Z. Feng, Z. Han, S. Gao, M.Y. Wang et al., Electrochemical and structural analysis in all-solid-state lithium batteries by analytical electron microscopy: progress and perspectives. *Adv. Mater.* **32**, 1903747 (2019). <https://doi.org/10.1002/adma.201903747>
113. H. Chen, D. Adekoya, L. Hencz, J. Ma, S. Chen et al., Stable seamless interfaces and rapid ionic conductivity of Ca-CeO₂/LiTFSI/PEO composite electrolyte for high-rate and high-voltage all-solid-state battery. *Adv. Energy Mater.* **10**, 2000049 (2020). <https://doi.org/10.1002/aenm.202000049>
114. H.H. Xu, P.H. Chien, J.J. Shi, Y.T. Lia, N. Wu et al., High-performance all-solid-state batteries enabled by salt bonding to perovskite in poly(ethylene oxide). *Proc. Natl. Acad. Sci. USA* **116**, 18815–18821 (2019). <https://doi.org/10.1073/pnas.1907507116>
115. X. Li, D.H. Wang, H.C. Wang, H.F. Yan, Z.L. Gong et al., Poly(ethylene oxide)-Li₁₀SnP₂S₁₂ composite polymer electrolyte enables high-performance all-solid-state lithium sulfur battery. *ACS Appl. Mater. Interfaces* **11**, 22745–22753 (2019). <https://doi.org/10.1021/acsaami.9b05212>



116. G. Piana, F. Bella, F. Geobaldo, G. Meligrana, C. Gerbaldi, PEO/LAGP hybrid solid polymer electrolytes for ambient temperature lithium batteries by solvent-free, “one pot” preparation. *J. Energy Storage* **26**, 100947 (2019). <https://doi.org/10.1016/j.est.2019.100947>
117. Z.P. Wan, D.N. Lei, W. Yang, C. Liu, K. Shi et al., Low resistance-integrated all-solid-state battery achieved by $\text{Li}_7\text{La}_3\text{Zr}_2\text{O}_{12}$ nanowire upgrading polyethylene oxide (PEO) composite electrolyte and PEO cathode binder. *Adv. Funct. Mater.* **29**, 1805301 (2019). <https://doi.org/10.1002/adfm.201805301>
118. Y.T. Li, B.Y. Xu, H.H. Xu, H.N. Duan, X.J. Lv et al., Hybrid polymer/garnet electrolyte with a small interfacial resistance for lithium-ion batteries. *Angew. Chem. Int. Ed.* **56**, 753–756 (2017). <https://doi.org/10.1002/anie.201608924>
119. M.R. Li, J.E. Frerichs, M. Kolek, W. Sun, D. Zhou et al., Solid-state lithium-sulfur battery enabled by thio-LiSICON/polymer composite electrolyte and sulfurized polyacrylonitrile cathode. *Adv. Funct. Mater.* **30**, 1910123 (2020). <https://doi.org/10.1002/adfm.201910123>
120. Z.Y. Huang, R.A. Tong, J. Zhang, L.H. Chen, C.A. Wang, Blending poly(ethylene oxide) and $\text{Li}_{6.4}\text{La}_3\text{Zr}_{1.4}\text{Ta}_{0.6}\text{O}_{12}$ by haake rheomixer without any solvent: a low-cost manufacture method for mass production of composite polymer electrolyte. *J. Power Sources* **451**, 227797 (2020). <https://doi.org/10.1016/j.jpowsour.2020.227797>
121. R.A. Tong, L.H. Chen, G. Shao, H.L. Wang, C.A. Wang, An integrated solvent-free modification and composite process of $\text{Li}_{6.4}\text{La}_3\text{Zr}_{1.4}\text{Ta}_{0.6}\text{O}_{12}$ /poly(ethylene oxide) solid electrolytes: enhanced compatibility and cycle performance. *J. Power Sources* **492**, 229672 (2021). <https://doi.org/10.1016/j.jpowsour.2021.229672>
122. R.A. Tong, H.L. Luo, L.H. Chen, J.X. Zhang, G. Shao et al., Constructing the lithium polymeric salt interfacial phase in composite solid-state electrolytes for enhancing cycle performance of lithium metal batteries. *Chem. Eng. J.* **442**, 136154 (2022). <https://doi.org/10.1016/j.cej.2022.136154>
123. Z.Y. Huang, W.Y. Pang, P. Liang, Z.H. Jin, N. Grundish et al., A dopamine modified $\text{Li}_{6.4}\text{La}_3\text{Zr}_{1.4}\text{Ta}_{0.6}\text{O}_{12}$ /PEO solid-state electrolyte: enhanced thermal and electrochemical properties. *J. Mater. Chem. A* **7**, 16425–16436 (2019). <https://doi.org/10.1039/c9ta03395e>
124. L. Chen, X.M. Qiu, Z.M. Bai, L.Z. Fan, Enhancing interfacial stability in solid-state lithium batteries with polymer/garnet solid electrolyte and composite cathode framework. *J. Energy Chem.* **52**, 210–217 (2021). <https://doi.org/10.1016/j.jechem.2020.03.052>
125. Y.L. Ni'mah, Z.H. Muhaiminah, S. Suprpto, Increase of solid polymer electrolyte ionic conductivity using Nano- SiO_2 synthesized from sugarcane bagasse as filler. *Polymers* **13**, 4240 (2021). <https://doi.org/10.3390/polym13234240>
126. X. Wang, H.W. Zhai, B.Y. Qie, Q. Cheng, A.J. Li et al., Rechargeable solid-state lithium metal batteries with vertically aligned ceramic nanoparticle/polymer composite electrolyte. *Nano Energy* **60**, 205–212 (2019). <https://doi.org/10.1016/j.nanoen.2019.03.051>
127. P. Pan, M.M. Zhang, Z.L. Cheng, L.Y. Jiang, J.T. Mao et al., Garnet ceramic fabric-reinforced flexible composite solid electrolyte derived from silk template for safe and long-term stable all-solid-state lithium metal batteries. *Energy Storage Mater.* **47**, 279–287 (2022). <https://doi.org/10.1016/j.ensm.2022.02.018>
128. R.G. Li, S.T. Guo, L. Yu, L.B. Wang, D.B. Wu et al., Morphosynthesis of 3D macroporous garnet frameworks and perfluorination of polymer-stabilized lithium salts for flexible solid-state hybrid electrolytes. *Adv. Mater. Interfaces* **6**, 1900200 (2019). <https://doi.org/10.1002/admi.201900200>
129. J.Q. Dai, K. Fu, Y.H. Gong, J.W. Song, C.J. Chen et al., Flexible solid-state electrolyte with aligned nanostructures derived from wood. *ACS Mater. Lett.* **1**, 354–361 (2019). <https://doi.org/10.1021/acsmaterialslett.9b00189>
130. Y.H. Gong, K. Fu, S.M. Xu, J.Q. Dai, T.R. Hamann et al., Lithium-ion conductive ceramic textile: a new architecture for flexible solid-state lithium metal batteries. *Mater. Today* **21**, 594–601 (2018). <https://doi.org/10.1016/j.mattod.2018.01.001>
131. S.D. Song, X.H. Qin, Y.L. Ruan, W.J. Li, Y.Q. Xu et al., Enhanced performance of solid-state lithium-air batteries with continuous 3D garnet network added composite polymer electrolyte. *J. Power Sources* **461**, 228146 (2020). <https://doi.org/10.1016/j.jpowsour.2020.228146>
132. X.L. Fu, Y.C. Li, C.Z. Liao, W.P. Gong, M.Y. Yang et al., Enhanced electrochemical performance of solid PEO/ LiClO_4 electrolytes with a 3D porous $\text{Li}_{6.28}\text{La}_3\text{Zr}_2\text{Al}_{0.24}\text{O}_{12}$ network. *Compos. Sci. Technol.* **184**, 107863 (2019). <https://doi.org/10.1016/j.compscitech.2019.107863>
133. C. Liu, J.X. Wang, W.J. Kou, Z.H. Yang, P.F. Zhai et al., A flexible, ion-conducting solid electrolyte with vertically bicontinuous transfer channels toward high performance all-solid-state lithium batteries. *Chem. Eng. J.* **404**, 126517 (2021). <https://doi.org/10.1016/j.cej.2020.126517>
134. S. Zekoll, C. Marriner-Edwards, A.K.O. Hekselman, J. Kasemchainan, C. Kuss et al., Hybrid electrolytes with 3D bicontinuous ordered ceramic and polymer microchannels for all-solid-state batteries. *Energy Environ. Sci.* **11**, 185–201 (2018). <https://doi.org/10.1039/c7ee02723k>
135. Z.Y. Wang, L. Shen, S.G. Deng, P. Cui, X.Y. Yao, 10 μm -thick high-strength solid polymer electrolytes with excellent interface compatibility for flexible all-solid-state lithium-metal batteries. *Adv. Mater.* **33**, 2100353 (2021). <https://doi.org/10.1002/adma.202100353>
136. H. Xie, C.P. Yang, K. Fu, Y.G. Yao, F. Jiang et al., Flexible, scalable, and highly conductive garnet-polymer solid electrolyte templated by bacterial cellulose. *Adv. Energy Mater.* **8**, 1703474 (2018). <https://doi.org/10.1002/aenm.201703474>
137. H.W. Zhai, P.Y. Xu, M.Q. Ning, Q. Cheng, J. Mandal et al., A flexible solid composite electrolyte with vertically aligned and connected ion-conducting nanoparticles for lithium batteries. *Nano Lett.* **17**, 3182–3187 (2017). <https://doi.org/10.1021/acs.nanolett.7b00715>

138. Y.H. Li, Z.Y. Fu, S.Y. Lu, X. Sun, X.R. Zhang et al., Polymer nanofibers framework composite solid electrolyte with lithium dendrite suppression for long life all-solid-state lithium metal battery. *Chem. Eng. J.* **440**, 135816 (2022). <https://doi.org/10.1016/j.cej.2022.135816>
139. M.M. Zhang, P. Pan, Z.L. Cheng, J.T. Mao, L.Y. Jiang et al., Flexible, mechanically robust, solid-state electrolyte membrane with conducting oxide-enhanced 3D nanofiber networks for lithium batteries. *Nano Lett.* **21**, 7070–7078 (2021). <https://doi.org/10.1021/acs.nanolett.1c01704>
140. Z.J. Zhang, Q. Wang, Z.H. Li, Y.C. Jiang, B. Zhao et al., Well-aligned BaTiO₃ nanofibers via solution blow spinning and their application in lithium composite solid-state electrolyte. *Mater. Express* **9**, 993–1000 (2019). <https://doi.org/10.1166/mex.2019.1589>
141. F. He, W.J. Tang, X.Y. Zhang, L.J. Deng, J.Y. Luo, High energy density solid state lithium metal batteries enabled by sub-5 μm solid polymer electrolytes. *Adv. Mater.* **33**, 2105329 (2021). <https://doi.org/10.1002/adma.202105329>
142. L.X. Gao, B. Tang, H.Y. Jiang, Z.J. Xie, J.P. Wei et al., Fiber-reinforced composite polymer electrolytes for solid-state lithium batteries. *Adv. Sustain. Syst.* **6**, 2100389 (2021). <https://doi.org/10.1002/adsu.202100389>
143. M.A. Navarra, L. Lombardo, P. Bruni, L. Morelli, A. Tsurumaki, S. Panero et al., Gel polymer electrolytes based on silica-added poly(ethylene oxide) electrospun membranes for lithium batteries. *Membranes* **8**, 126 (2018). <https://doi.org/10.3390/membranes8040126>
144. J.W. Zha, N. Huang, K.Q. He, Z.M. Dang, C.Y. Shi et al., Electrospun poly(ethylene oxide) nanofibrous composites with enhanced ionic conductivity as flexible solid polymer electrolytes. *High Volt.* **2**, 25–31 (2017). <https://doi.org/10.1049/hve.2016.0069>
145. W. Liu, N. Liu, J. Sun, P.C. Hsu, Y.Z. Li et al., Ionic conductivity enhancement of polymer electrolytes with ceramic nanowire fillers. *Nano Lett.* **15**, 2740–2745 (2015). <https://doi.org/10.1021/acs.nanolett.5b00600>
146. K. Fu, Y.H. Gong, J.Q. Dai, A. Gong, X.G. Han et al., Flexible, solid-state, ion-conducting membrane with 3D garnet nanofiber networks for lithium batteries. *Proc. Natl. Acad. Sci. USA* **113**, 7094–7099 (2016). <https://doi.org/10.1073/pnas.1600422113>
147. X.Z. Wang, Y.B. Zhang, X. Zhang, T. Liu, Y.H. Lin et al., Lithium-salt-rich PEO/Li_{0.3}La_{0.557}TiO₃ interpenetrating composite electrolyte with three-dimensional ceramic nano-backbone for all-solid-state lithium-ion batteries. *ACS Appl. Mater. Interfaces* **10**, 24791–24798 (2018). <https://doi.org/10.1021/acsami.8b06658>
148. J.M. Yu, C. Wang, S.H. Li, N. Liu, J. Zhu et al., Li⁺-containing, continuous silica nanofibers for high Li⁺ conductivity in composite polymer electrolyte. *Small* **15**, 1902729 (2019). <https://doi.org/10.1002/smll.201902729>
149. J.Y. Wan, J. Xie, X. Kong, Z. Liu, K. Liu et al., Ultrathin, flexible, solid polymer composite electrolyte enabled with aligned nanoporous host for lithium batteries. *Nat. Nanotechnol.* **14**, 705–711 (2019). <https://doi.org/10.1038/s41565-019-0465-3>
150. Y. Cui, J.Y. Wan, Y.S. Ye, K. Liu, L.Y. Chou et al., A fire-proof, lightweight, polymer-polymer solid-state electrolyte for safe lithium batteries. *Nano Lett.* **20**, 1686–1692 (2020). <https://doi.org/10.1021/acs.nanolett.9b04815>
151. J.Y. Wu, Z.X. Rao, Z.X. Cheng, L.X. Yuan, Z. Li et al., Ultrathin, flexible polymer electrolyte for cost-effective fabrication of all-solid-state lithium metal batteries. *Adv. Energy Mater.* **9**, 1902767 (2019). <https://doi.org/10.1002/aenm.201902767>
152. J. Bae, Y.T. Li, J. Zhang, X.Y. Zhou, F. Zhao et al., A 3D nanostructured hydrogel-framework-derived high-performance composite polymer lithium-ion electrolyte. *Angew. Chem. Int. Ed.* **57**, 2096–2100 (2018). <https://doi.org/10.1002/anie.201710841>
153. J. Bae, Y.T. Li, F. Zhao, X.Y. Zhou, Y. Ding et al., Designing 3D nanostructured garnet frameworks for enhancing ionic conductivity and flexibility in composite polymer electrolytes for lithium batteries. *Energy Storage Mater.* **15**, 46–52 (2018). <https://doi.org/10.1016/j.ensm.2018.03.016>
154. M. Falco, L. Castro, J.R. Nair, F. Bella, F. Bardé et al., UV-cross-linked composite polymer electrolyte for high-rate, ambient temperature lithium batteries. *ACS Appl. Energy Mater.* **2**, 1600–1607 (2019). <https://doi.org/10.1021/acsaeam.8b02185>
155. S.H. Siyal, M.S. Javed, A.H. Jatoi, J.L. Lan, Y.H. Yu et al., In situ curing technology for dual ceramic composed by organic-inorganic functional polymer gel electrolyte for dendritic-free and robust lithium-metal batteries. *Adv. Mater. Interfaces* **7**, 2000830 (2020). <https://doi.org/10.1002/admi.202000830>
156. S.H. Siyal, M.J. Li, H. Li, J.L. Lan, Y.H. Yu et al., Ultraviolet irradiated PEO/LATP composite gel polymer electrolytes for lithium-metallic batteries (LMBs). *Appl. Surf. Sci.* **494**, 1119–1126 (2019). <https://doi.org/10.1016/j.apsusc.2019.07.179>
157. J. Shi, H.G. Xiong, Y.F. Yang, H.X. Shao, Nano-sized oxide filled composite PEO/PMMA/P(VDF-HFP) gel polymer electrolyte for rechargeable lithium and sodium batteries. *Solid State Ion.* **326**, 136–144 (2018). <https://doi.org/10.1016/j.ssi.2018.09.019>
158. Y.T. Wang, J.W. Ju, S.M. Dong, Y.Y. Yan, F. Jiang et al., Facile design of sulfide-based all solid-state lithium metal battery: In situ polymerization within self-supported porous argyrodite skeleton. *Adv. Funct. Mater.* **31**, 2101523 (2021). <https://doi.org/10.1002/adfm.202101523>
159. R.L. Wang, Q. Dong, C.W. Wang, M. Hong, J.L. Gao et al., High-temperature ultrafast sintering: Exploiting a new kinetic region to fabricate porous solid-state electrolyte scaffolds. *Adv. Mater.* **33**, 2100726 (2021). <https://doi.org/10.1002/adma.202100726>
160. K. Zhang, F. Wu, X.R. Wang, S.T. Weng, X.Y. Yang et al., 8.5 μm-thick flexible-rigid hybrid solid-electrolyte/lithium integration for air-stable and interface-compatible



- all-solid-state lithium metal batteries. *Adv. Energy Mater.* **12**, 2200368 (2022). <https://doi.org/10.1002/aenm.20220368>
161. J. Yu, X.D. Lin, J.P. Liu, J.T.T. Yu, M.J. Robson et al., In situ fabricated quasi-solid polymer electrolyte for high-energy-density lithium metal battery capable of subzero operation. *Adv. Energy Mater.* **12**, 2102932 (2021). <https://doi.org/10.1002/aenm.202102932>
162. Y. Chen, F. Huo, S.M. Chen, W.B. Cai, S.J. Zhang, In-built quasi-solid-state poly-ether electrolytes enabling stable cycling of high-voltage and wide-temperature Li metal batteries. *Adv. Funct. Mater.* **31**, 2102347 (2021). <https://doi.org/10.1002/adfm.202102347>
163. D.L. Chen, T. Zhu, M. Zhu, S.Q. Yuan, P.B. Kang et al., In-situ constructing “ceramer” electrolytes with robust-flexible interfaces enabling long-cycling lithium metal batteries. *Energy Storage Mater.* (2022). <https://doi.org/10.1016/j.ensm.2022.09.022>
164. J.X. Yang, X. Liu, Y. Wang, X.W. Zhou, L.T. Weng et al., Electrolytes polymerization-induced cathode-electrolyte-interphase for high voltage lithium-ion batteries. *Adv. Energy Mater.* **11**, 2101956 (2021). <https://doi.org/10.1002/aenm.202101956>
165. H. Shen, E. Yi, S. Heywood, D.Y. Parkinson, G.Y. Chen et al., Scalable freeze-tape-casting fabrication and pore structure analysis of 3D LLZO solid-state electrolytes. *ACS Appl. Mater. Interfaces* **12**, 3494–3501 (2020). <https://doi.org/10.1021/acsami.9b11780>
166. E. Yi, H. Shen, S. Heywood, J. Alvarado, D.Y. Parkinson et al., All-solid-state batteries using rationally designed garnet electrolyte frameworks. *ACS Appl. Energy Mater.* **3**, 170–175 (2020). <https://doi.org/10.1021/acsaem.9b02101>
167. T.L. Jiang, P.G. He, G.X. Wang, Y. Shen, C.W. Nan et al., Solvent-free synthesis of thin, flexible, nonflammable garnet-based composite solid electrolyte for all-solid-state lithium batteries. *Adv. Energy Mater.* **10**, 1903376 (2020). <https://doi.org/10.1002/aenm.201903376>
168. J.J. Xu, Critical review on cathode-electrolyte interphase toward high-voltage cathodes for Li-ion batteries. *Nanomicro Lett.* **14**, 166 (2022). <https://doi.org/10.1007/s40820-022-00917-2>
169. O.W. Sheng, C.P. Jin, J.M. Luo, H.D. Yuan, C. Fang et al., Ionic conductivity promotion of polymer electrolyte with ionic liquid grafted oxides for all-solid-state lithium-sulfur batteries. *J. Mater. Chem. A* **5**, 12934–12942 (2017). <https://doi.org/10.1039/c7ta03699j>
170. J. Cao, L. Wang, X.M. He, M. Fang, J. Gao et al., In situ prepared nano-crystalline TiO₂-poly(methyl methacrylate) hybrid enhanced composite polymer electrolyte for Li-ion batteries. *J. Mater. Chem. A* **1**, 5955–5961 (2013). <https://doi.org/10.1039/c3ta00086a>
171. H.Y. Huo, N. Zhao, J.Y. Sun, F.M. Du, Y.Q. Li et al., Composite electrolytes of polyethylene oxides/garnets interfacially wetted by ionic liquid for room-temperature solid-state lithium battery. *J. Power Sources* **372**, 1–7 (2017). <https://doi.org/10.1016/j.jpowsour.2017.10.059>
172. F.D. Han, A.S. Westover, J. Yue, X.L. Fan, F. Wang et al., High electronic conductivity as the origin of lithium dendrite formation within solid electrolytes. *Nat. Energy* **4**, 187–196 (2019). <https://doi.org/10.1038/s41560-018-0312-z>
173. E. Kuhnert, L. Ladenstein, A. Jodlbauer, C. Slugovc, G. Trimmel et al., Lowering the interfacial resistance in Li_{6,4}La₃Zr_{1,4}Ta_{0,6}O₁₂/poly(ethylene oxide) composite electrolytes. *Cell Rep. Phys. Sci.* **1**, 100214 (2020). <https://doi.org/10.1016/j.xcrp.2020.100214>
174. Y.H. Zhu, J. Cao, H. Chen, Q.P. Yu, B.H. Li, High electrochemical stability of 3D cross-linked network PEO@nano-SiO₂ composite polymer electrolyte for lithium metal batteries. *J. Mater. Chem. A* **7**, 6832–6839 (2013). <https://doi.org/10.1039/C9TA00560A>
175. Y. Kim, S.J. Kwon, H.K. Jang, B.M. Jung, S.B. Lee et al., High ion conducting nanohybrid solid polymer electrolytes via single-ion conducting mesoporous organosilica in poly(ethylene oxide). *Chem. Mater.* **29**, 4401–4410 (2017). <https://doi.org/10.1021/acs.chemmater.7b00879>
176. S. Choudhury, S. Stalin, Y. Deng, L.A. Archer, Soft colloidal glasses as solid-state electrolytes. *Chem. Mater.* **30**, 5996–6004 (2018). <https://doi.org/10.1021/acs.chemmater.8b02227>
177. D.C. Lin, W. Liu, Y.Y. Liu, H.R. Lee, P.C. Hsu et al., High ionic conductivity of composite solid polymer electrolyte via in situ synthesis of monodispersed SiO₂ nanospheres in poly(ethylene oxide). *Nano Lett.* **16**, 459–465 (2016). <https://doi.org/10.1021/acs.nanolett.5b04117>
178. X.J. Tan, Y.M. Wu, W.P. Tang, S.F. Song, J.Y. Yao et al., Preparation of nanocomposite polymer electrolyte via in situ synthesis of SiO₂ nanoparticles in PEO. *Nanomaterials* **10**, 157 (2020). <https://doi.org/10.3390/nano10010157>
179. K.C. Pan, L. Zhang, W.W. Qian, X.K. Wu, K. Dong et al., A flexible ceramic/polymer hybrid solid electrolyte for solid-state lithium metal batteries. *Adv. Mater.* **32**, 2000399 (2020). <https://doi.org/10.1002/adma.202000399>
180. W.D. Bao, L.Q. Zhao, H.J. Zhao, L.X. Su, X.C. Cai et al., Vapor phase infiltration of ZnO quantum dots for all-solid-state PEO-based lithium batteries. *Energy Storage Mater.* **43**, 258–265 (2021). <https://doi.org/10.1016/j.ensm.2021.09.010>
181. X.N. Ma, Y.L. Xu, B.F. Zhang, X. Xue, C. Wang et al., Garnet Si-Li₇La₃Zr₂O₁₂ electrolyte with a durable, low resistance interface layer for all-solid-state lithium metal batteries. *J. Power Sources* **453**, 227881 (2020). <https://doi.org/10.1016/j.jpowsour.2020.227881>
182. L.H. Chen, J. Zhang, R.A. Tong, J.X. Zhang, H.L. Wang et al., Excellent Li/garnet interface wettability achieved by porous hard carbon layer for solid state Li metal battery. *Small* **18**, e2106142 (2022). <https://doi.org/10.1002/sml.202106142>
183. K. Liu, R.H. Zhang, J. Sun, M.C. Wu, T.S. Zhao, Polyoxyethylene (PEO)∥PEO–Perovskite∥PEO composite electrolyte for all-solid-state lithium metal batteries. *ACS Appl. Mater.*

- Interfaces **11**, 46930–46937 (2019). <https://doi.org/10.1021/acsami.9b16936>
184. J.N. Liang, Q. Sun, Y. Zhao, Y.P. Sun, C.H. Wang et al., Stabilization of all-solid-state Li-S batteries with a polymer-ceramic sandwich electrolyte by atomic layer deposition. *J. Mater. Chem. A* **6**, 23712–23719 (2018). <https://doi.org/10.1039/c8ta09069f>
185. L.H. Chen, Y.B. Su, J. Zhang, H.J. Zhang, B.B. Fan et al., Nanosecond laser cleaning method to reduce the surface inert layer and activate the garnet electrolyte for a solid-state Li metal battery. *ACS Appl. Mater. Interfaces* **13**, 37082–37090 (2021). <https://doi.org/10.1021/acsami.1c08509>
186. H.C. Yang, Y.M. Zhang, M.J. Tennenbaum, Z. Althouse, Y. Ma et al., Polypropylene carbonate-based adaptive buffer layer for stable interfaces of solid polymer lithium metal batteries. *ACS Appl. Mater. Interfaces* **11**, 27906–27912 (2019). <https://doi.org/10.1021/acsami.9b08285>
187. C.H. Wang, G.L. Bai, Y.F. Yang, X.J. Liu, H.X. Shao, Dendrite-free all-solid-state lithium batteries with lithium phosphorous oxynitride-modified lithium metal anode and composite solid electrolytes. *Nano Res.* **12**, 217–223 (2019). <https://doi.org/10.1007/s12274-018-2205-7>
188. W.D. Zhou, Z.X. Wang, Y. Pu, Y.T. Li, S. Xin et al., Double-layer polymer electrolyte for high-voltage all-solid-state rechargeable batteries. *Adv. Mater.* **31**, 1805574 (2018). <https://doi.org/10.1002/adma.201805574>
189. S.Z. Zhang, T.B. Liang, D.H. Wang, Y.J. Xu, Y.L. Cui et al., A stretchable and safe polymer electrolyte with a protecting-layer strategy for solid-state lithium metal batteries. *Adv. Sci.* **8**, 2003241 (2021). <https://doi.org/10.1002/advs.202003241>
190. X.Y. Xu, Y.Y. Liu, O.O. Kapitanova, Z.X. Song, J. Sun et al., Electro-chemo-mechanical failure of solid electrolytes induced by growth of internal lithium filaments. *Adv. Mater.* **34**, 2207232 (2022). <https://doi.org/10.1002/adma.202207232>
191. Y.Y. Liu, X.Y. Xu, O.O. Kapitanova, P.V. Evdokimov, Z.X. Song et al., Electro-chemo-mechanical modeling of artificial solid electrolyte interphase to enable uniform electrodeposition of lithium metal anodes. *Adv. Energy Mater.* **12**, 2103589 (2022). <https://doi.org/10.1002/aenm.202103589>
192. L. Liu, L. Yang, M. Liu, X.Y. Wang, X.L. Li et al., A flexible tysonite-type $\text{La}_{0.95}\text{Ba}_{0.05}\text{F}_{2.95}$ @PEO-based composite electrolyte for the application of advanced fluoride ion battery. *J. Energy Storage* **25**, 100886 (2019). <https://doi.org/10.1016/j.est.2019.100886>
193. X.F. Yang, M. Jiang, X.J. Gao, D.N. Bao, Q. Sun et al., Determining the limiting factor of the electrochemical stability window for PEO-based solid polymer electrolytes: main chain or terminal –OH group? *Energy Environ. Sci.* **13**, 1318–1325 (2020). <https://doi.org/10.1039/d0ee00342e>
194. R. Fan, W.C. Liao, S.X. Fan, D.Z. Chen, J.N. Tang et al., Regulating interfacial Li-ion transport via an integrated corrugated 3D skeleton in solid composite electrolyte for all-solid-state lithium metal batteries. *Adv. Sci.* **9**, 2104506 (2022). <https://doi.org/10.1002/advs.202104506>
195. S.J. Liu, H.R. Shan, S.H. Xia, J.H. Yan, J.Y. Yu et al., Polymer template synthesis of flexible SiO_2 nanofibers to upgrade composite electrolytes. *ACS Appl. Mater. Interfaces* **12**, 31439–31447 (2020). <https://doi.org/10.1021/acsami.0c06922>
196. J.Q. Sun, C.H. He, X.M. Yao, A.Q. Song, Y.G. Li et al., Hierarchical composite-solid-electrolyte with high electrochemical stability and interfacial regulation for boosting ultra-stable lithium batteries. *Adv. Funct. Mater.* **31**, 2006381 (2020). <https://doi.org/10.1002/adfm.202006381>
197. X. Wen, Q.H. Zeng, J.Z. Guan, W. Wen, P.P. Chen et al., 3D structural lithium alginate-based gel polymer electrolytes with superior high-rate long cycling performance for high-energy lithium metal batteries. *J. Mater. Chem. A* **10**, 707–718 (2022). <https://doi.org/10.1039/d1ta07252h>
198. J. Lopez, D.G. Mackanic, Y. Cui, Z.N. Bao, Designing polymers for advanced battery chemistries. *Nat. Rev. Mater.* **4**, 312–330 (2019). <https://doi.org/10.1038/s41578-019-0103-6>
199. X. Judez, H. Zhang, C.M. Li, G.G. Eshetu, Y. Zhang et al., Polymer-rich composite electrolytes for all-solid-state Li-S cells. *J. Phys. Chem. Lett.* **8**, 3473–3477 (2017). <https://doi.org/10.1021/acs.jpcclett.7b01321>
200. R.Y. Fang, H.H. Xu, B.Y. Xu, X.Y. Li, Y.T. Li et al., Reaction mechanism optimization of solid-state Li–S batteries with a PEO-based electrolyte. *Adv. Funct. Mater.* **31**, 2001812 (2020). <https://doi.org/10.1002/adfm.202001812>
201. F. Lee, M.C. Tsai, M.H. Lin, Y.L. Ni'mah, S. Hy et al., Capacity retention of lithium sulfur batteries enhanced with nano-sized TiO_2 -embedded polyethylene oxide. *J. Mater. Chem. A* **5**, 6708–6715 (2017). <https://doi.org/10.1039/c6ta10755a>
202. X.Y. Tao, Y.Y. Liu, W. Liu, G.M. Zhou, J. Zhao et al., Solid-state lithium–sulfur batteries operated at 37 °C with composites of nanostructured $\text{Li}_7\text{La}_3\text{Zr}_2\text{O}_{12}$ /carbon foam and polymer. *Nano Lett.* **17**, 2967–2972 (2017). <https://doi.org/10.1021/acs.nanolett.7b00221>
203. Y.B. Zhang, R.J. Chen, S. Wang, T. Liu, B.Q. Xu et al., Free-standing sulfide/polymer composite solid electrolyte membranes with high conductance for all-solid-state lithium batteries. *Energy Storage Mater.* **25**, 145–153 (2020). <https://doi.org/10.1016/j.ensm.2019.10.020>

